FIRST-PRINCIPLES STUDY OF LANTHANUM MANGANITE ($LaMnO_3$)

by

BAYILEYEGN AKANIE

A thesis submitted in partial fulfillment of the requirement for the degree of Master of Science in Materials Science at Addis Ababa University School of Graduate Studies

Addis Ababa, Ethiopia

March, 2010

Acknowledgments

I am immensely indebted to Prof. Nicola Marzari for his unusual generosity and understanding.

I would like to express my heartfelt thanks to Dr. S. K. Ghoshal for his unconditional support, guidance, and teaching during my graduate studies and this thesis.

I am very much grateful to Prof. Teketel Yohannes for encouraging and assisting me to finish this work.

I am thankful to Mrs. Belaynesh and Ms. Beza for their continued cooperation during my studies and this thesis.

Thank you friends.

Table of Contents

List of Tables

List of Figures

Abstract

In this thesis, we have investigated the structural, electronic, and magnetic properties of pure $LaMnO_3$ from first-principles using the quantum-ESPRESSO open-source code. Unlike previous theoretical works, most of which implemented experimental structure, we have performed full structural relaxations for both the cubic and orthorhombic structures within the GGA and LDA+U approaches. Our simulated structural parameters are in very good agreement with experimental values. We have used these theoretical geometries in all the calculations. Consistent with the general theory of the CMR manganites but not reported in earlier theoretical works, the band structure and DOS calculations for the cubic ferroelectric phase predict half-metallicity. We have also examined the phonon-dispersion and the corresponding density of states for the theoretically optimized cubic ferromagnetic $LaMnO_3$ from which we are able to observe two strong crystal instabilities. The phonon dispersion is calculated along the high-symmetry axes throughout the Brillouin zone. The densities of states calculated for the orthorhombic structure with different magnetic orderings strongly suggest the need for structural relaxation in order to get the experimentally observed insulating ground state for $LaMnO_3$. Both GGA and LDA+U calculations for the fully relaxed orthorhombic A-type antiferromagnetic structure reproduce the insulating character. However, the value of the insulating gap obtained within the LDA+U case is much closer to experiment than that of GGA, which in turn means that a better description of $LaMnO_3$ is possible with the inclusion of the on-site coulomb interaction.

Declaration

This thesis is my original work and has not been presented for a degree in any university.

Name: _____

Signature: _____

This thesis has been submitted for examination with my approval as a university advisor.

_____

Dr. S. K. Ghoshal

_____

Date

CHAPTER 1

Introduction

1.1 Perovskite manganites

The study of perovskite manganites has been undergoing intensive development, not only because these materials have great potential in applications related to the colossal magnetoresistance (CMR) effect [1, 2], but also because they offer a testing ground for theories related to strongly correlated systems. Subsequent studies of the manganites following the remarkable discovery of the CMR effect have showed that this family is indeed home to very diverse, unusual, and poorly understood phenomena as well as phases [3]. Depending on temperature, composition, and magnetic field, manganites can have various ground states. They show insulating states, which can be paramagnetic, ferromagnetic, or antiferromagnetic. What is strange and most exotic about these solid-state oxides is that, even in a single crystal sample of high chemical purity, different phases having different electronic and magnetic properties can coexist at different locations in the sample [4, 5]. Thus, manganites have an intrinsic electronic inhomogeneity, which can evolve on application of external stimuli like temperature and magnetic field.

The complex manganites to which the colossal magnetoresistive manganites belong are derived from a structure that consists on a lattice of oxygen octahedra with Mn in their center. They have the general chemical formula: $R_{1-x}D_xMnO_3$, where R is a rare earth element (La, Pr, Nd, etc.) and D is a divalent metal (Ca, Sr, Ba, etc.) [6, 7].

Structurally, manganites belong to the perovskite family [8] with the general chemical formula ABO_3, which can be viewed as corner-sharing octahedra with the manganese ion at the center of the MnO_6 octahedron, the oxygen ions at the corner, and the A ions in the interstitial space between the octahedra. Figure 1.1 shows the typical perovskite structure. An important structural feature of the perovskite manganites is the presence of the MnO_6 octahedra, which may be distorted. $LaMnO_3$ and $CaMnO_3$, for instance, are stabilized in the orthorhombic crystal structure, which is a distorted form of the cubic perovskite structure (fig. 1.2).

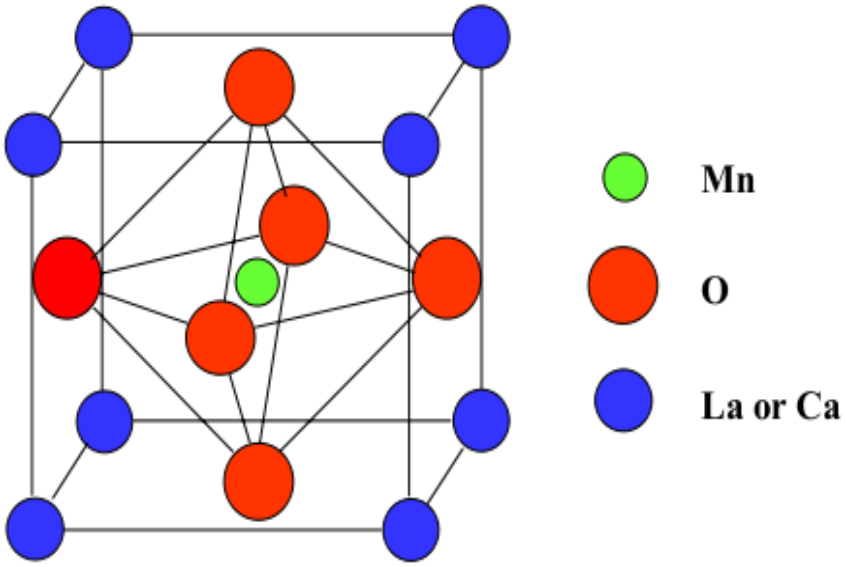

Figure 1.1. Sketch of the cubic perovskite unit cell for manganites. Lanthanum and calcium occupy the A-sites and manganese occupies the central B-site. (Taken from [9]).

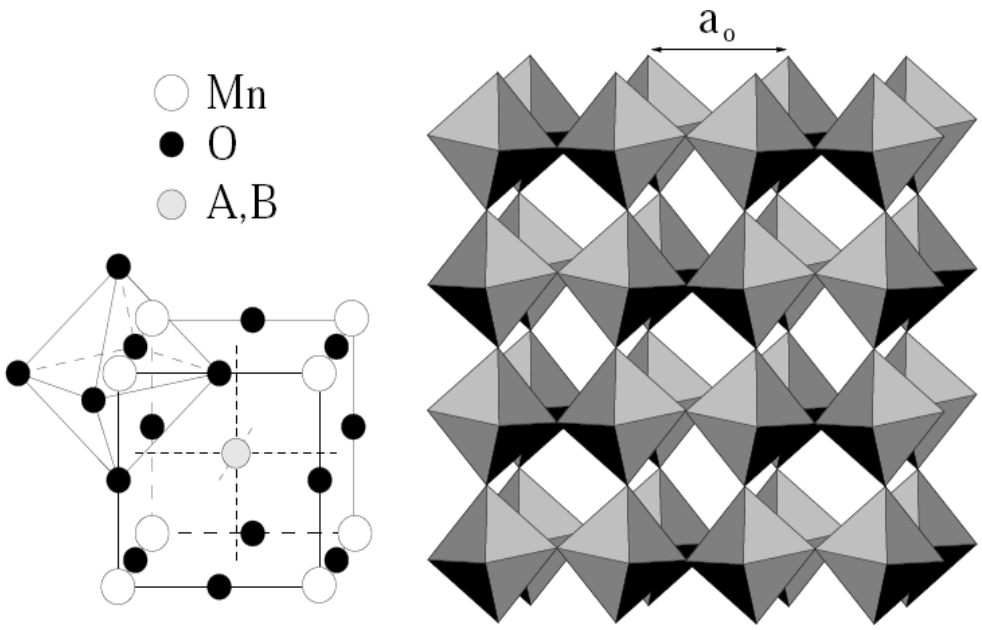

Figure1.2. Manganites' cubic crystalline structure. (Taken from [8]).

Six oxygens on the vertices and one manganese in their center form the octahedra. The octahedra are slightly tilted due to ionic size mismatch between A and B cations. The lattice parameter a_0 depends on the exact chemical composition.

1.2 Important interactions in manganites

Manganites are characterized by the coexistence of several interactions on comparable energy scales, which produce a complex interplay of magnetism, electron-lattice coupling, orbital and charge ordering [6, 10]. Three strong interactions, namely large on-site Coulomb repulsion, strong Jahn-Teller coupling, and large ferromagnetic Hund's rule coupling are the main driving force of the unusual properties exhibited by the manganites.

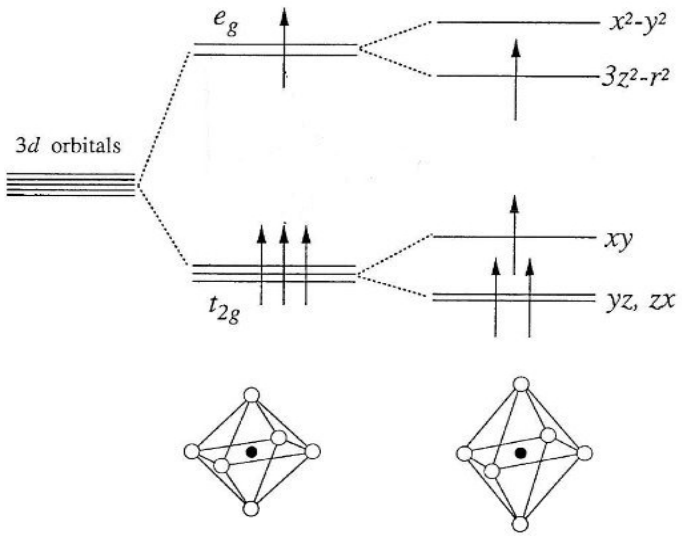

Figure 1.3. The energy levels of the 3d electrons of Mn^{3+}. (Taken from [10]).

In a cubic crystal field, the fivefold degeneracy of the atomic 3d levels is lifted to three lower t_{2g} and two higher e_g levels. The particular Jahn-Teller distortion shown leads to a further splitting of both the t_{2g} and e_g states and removes the degeneracy as shown in fig. 1.3.

The crystal field due to the surrounding oxygen octahedron splits the fivefold degenerate Mn 3d orbitals into a triplet of t_{2g} orbitals which have their lobes pointing between the oxygen ions and a doublet of e_g orbitals [4, 10]. As a result of the electrostatic repulsion between the electronic clouds, the t_{2g} levels lie lower in energy than the e_g ones. Three electrons occupy the low-lying localized t_{2g} orbitals and lock into a 'core spin' with (S = 3/2) due to strong Hund's coupling. The two e_g orbitals are partially occupied by 1-x electrons per manganese ion. A strong on-site Hund's coupling interaction splits the up-and down-spin orbitals by an amount comparable to or slightly larger than the crystal-field splitting. The Hund's rule aligns all the d electrons parallel to each other [11] as a result of which the total spins of the Mn^{3+} and Mn^{4+} ions become $2\mu_B$ and $3/2\mu_B$, respectively.

1.3 The colossal magnetoresistance effect

Manganites are important from the technological point of view because of the colossal magnetoresistance (CMR) effect. This extraordinary property has played a crucial role in revolutionizing materials science. It's also believed by a grate majority of the scientific society that the CMR effect could be the key to the next generation of magnetic memory devices, magnetic-filed sensors, or transistors [11].

Magnetoresistance (MR), a property of magnetic materials, is defined as the change in the electrical resistance produced by the application of an external magnetic field. Mathematically is given by [11]:

$$MR = \frac{\rho(H) - \rho(H = 0)}{\rho(H = 0)} \tag{1.1}$$

where ρ is the resistivity.

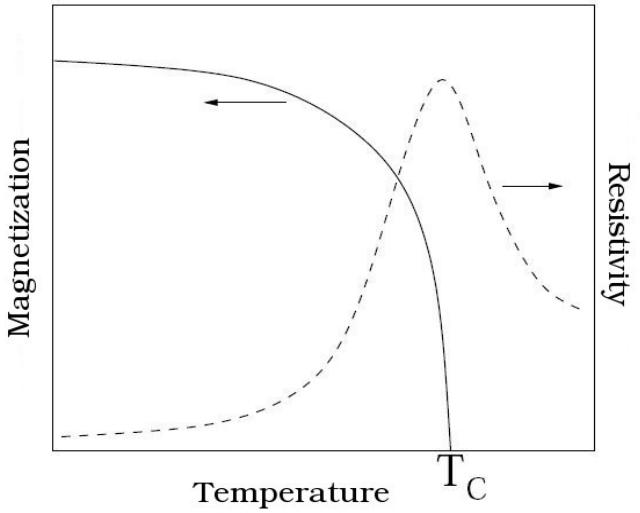

Figure 1.4. Correlation between ferromagnetism and metallicity in manganites. (Taken from [8]).

Hole-doped manganites exhibit very large negative magnetoresistance [8]: when magnetic field is applied, the peak on the resistivity moves toward higher temperature and dramatically decreases its height. The maximum intrinsic MR in these materials, caused by intrinsic interactions, is observed close to the ferromagnetic-paramagnetic transition. Typical intrinsic effects are due to the alignment of atomic spins and may only become significant in fields of several tesla, whereas extrinsic effects originate in the alignment of magnetic domains and can be seen in fields of a few millitesla.

Owing to their exhibition of the CMR effect, $La_{1-x}Ca_xMnO_3$ and $La_{1-x}Sr_xMnO_3$ are the two most intensively studied systems of the family [4, 8, 10]. These mixed-valence manganites show a metal-insulator transition, which is associated with unusual transport properties, including the large magnetoresistance in the vicinity of the transition. A qualitatively correct picture of the CMR effect is provided by Zener's double exchange mechanism [12]. According to this mechanism, the alignment of adjacent localized t_{2g} spins on Mn^{3+} and Mn^{4+} rules the dynamics of e_g electrons.

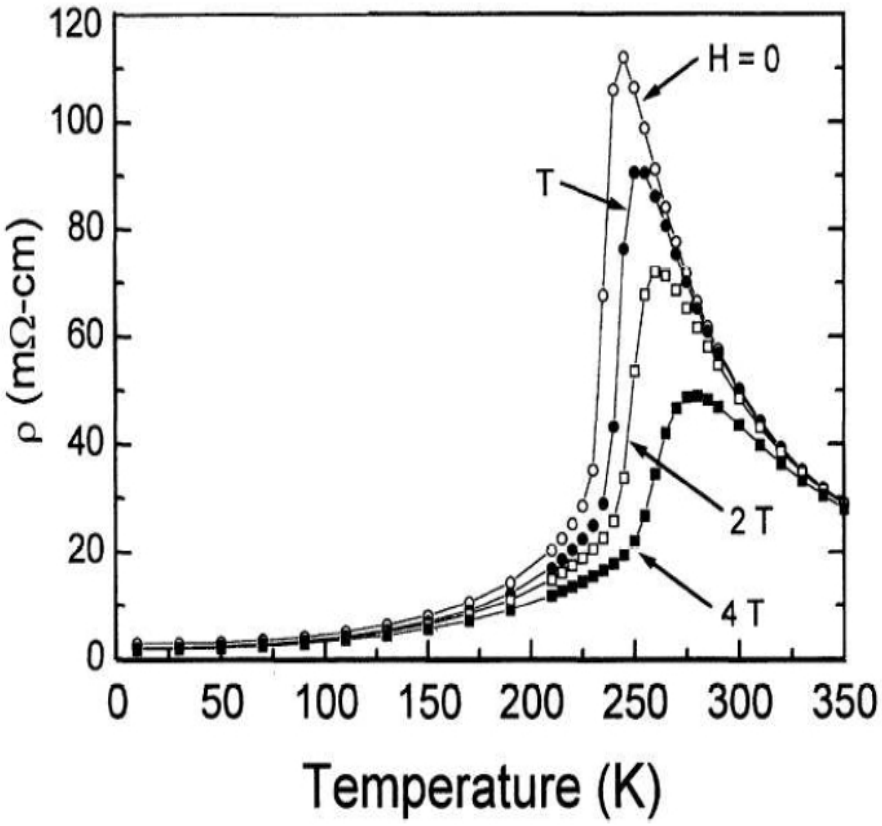

Figure.1.5. Colossal magnetoresistance observed in $La_{0.75}Ca_{0.25}MnO_3$ sample with a Curie temperature T_c of about 230K. (Taken from [4]).

The resistivity of $La_{0.75}Ca_{0.25}MnO_3$, shown in fig. 1.5, as a function of temperature for various values of magnetic fields, exhibits two different regimes: insulating at high temperature and metallic at low temperature. The critical temperature T_c at which this switchover occurs increases upon application of a magnetic field. At a fixed temperature, in the vicinity of T_c application of a magnetic filed of few tesla produces a drop of several orders of magnitude in the resistivity, signifying the name colossal magnetoresistance.

1.4 Lanthanum manganite

Among the manganese oxides, lanthanum manganite ($LaMnO_3$) is particularly important because it is the parent compound of the family of the manganites which exhibit the CMR effect [6, 12, 13]. Therefore, a through understanding of this material is indeed a prerequisite to achieve a better understanding of the family.

$LaMnO_3$ exhibits rich and interesting physical properties related to a strong interplay between lattice distortions, transport properties, and magnetic ordering. In stoichiometric $LaMnO_3$, in which all the manganese ions are formally in the Mn^{3+} oxidation state, the electronic configuration of Mn^{3+} is postulated as $t^{3\uparrow}_{2g}e^{1\uparrow}_{g}$. This electronic configuration is susceptible to a strong JT distortion [14, 15] which breaks the local octahedral symmetry and removes the twofold degeneracy of the e_g states. The JT distortion can be looked upon as a cooperative shifting of the oxygens within the *ab* plane away from one of its two nearest-neighboring manganese atoms toward the others, thereby creating long and short Mn-O bond lengths. The bond lengths are modified from 1.97Å for the cubic lattice to 1.91Å, 1.96Å, and 2.18Å for the orthorhombic variant [13].

At ambient conditions, experimental studies using x-ray and neutron-diffraction techniques show that $LaMnO_3$, stabilized in the orthorhombic variant of the cubic perovskite structure, is an insulator. The orthorhombic structure comprises four formula units (20 atoms) and can be viewed as a highly distorted cubic perovskite structure with experimental lattice parameters a=5.5367, b=5.7473, and c=7.6929Å [16]. Effects like, a strong Jahn-teller distortion as well as mutual tilting and rotation of the MnO_6 octahedra are characteristic to the orthorhombic structure. The tilting of the MnO_6 octahedra which is attributed to the relative sizes of the constituents changes the Mn-O-Mn bond angle from 180^0 to ~160^0, while its rotation facilitates a more efficient space filling. Neglect of these effects transforms the structure into a tetragonal one. At high temperature (above 750 K) $LaMnO_3$ undergoes a transition from the JT distorted orthorhombic phase to the perovskite structure, which is nearly cubic. Figure 1.6 shows the low- and high-temperature structures of $LaMnO_3$.

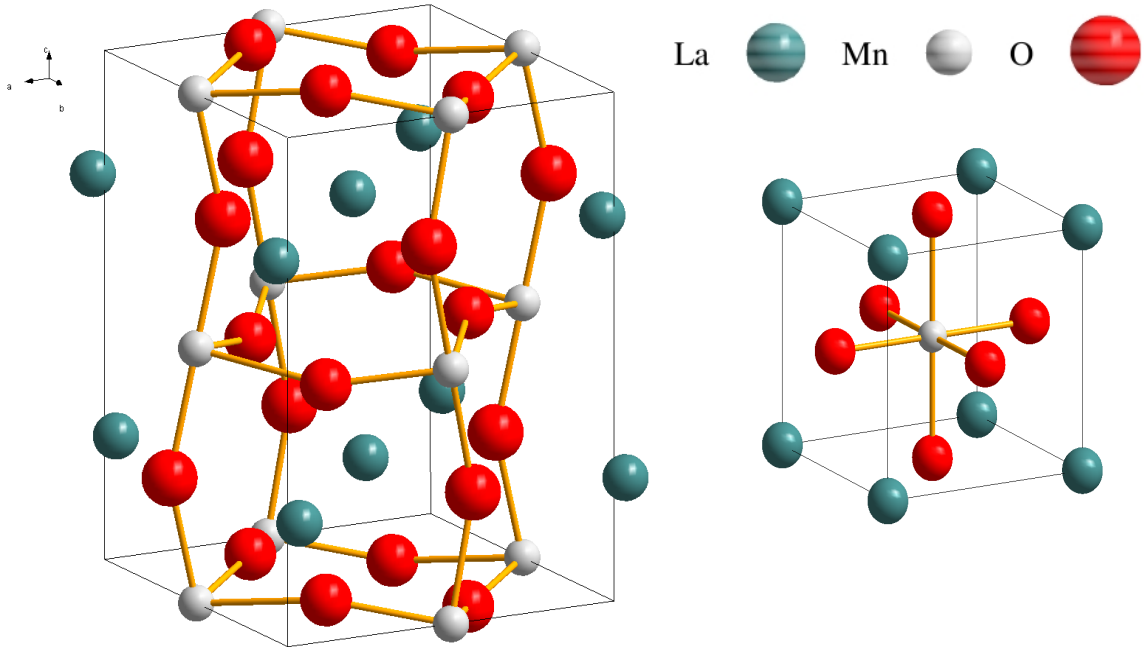

(a) Orthorhombic (b) Cubic

Figure 1.6. (a) Low- and (b) High-temperature structures of $LaMnO_3$. (Taken from [16]).

Depending on the four Mn spin orientations in the orthorhombic unit cell of 20 atoms, there are four possible magnetic orderings [10]: ferromagnetic (FM), as well as A-, C-, and G-type antiferromagnetic (A-AF, C-AF, and G-AF). Below T_N=140 K, the Jahn-Teller distortion accompanied by the A-type AF configuration is the lowest energy.

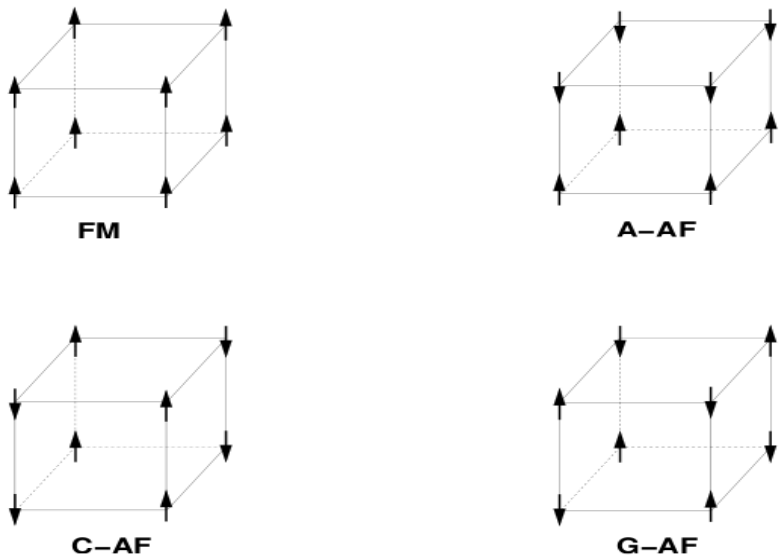

Figure 1.7. Schematic representation of the four types of magnetic orderings. The up and down arrows represent the up and down spin orientations in the magnetic case. (Taken from [10])

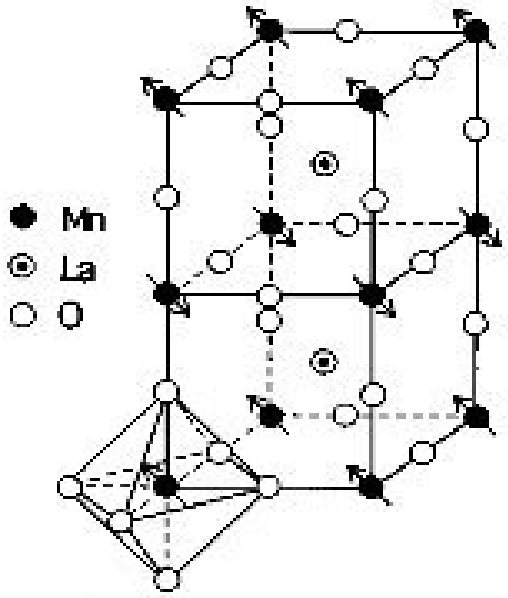

Figure 1.8. The ideal cubic perovskite structure, showing the A-type antiferromagnetic ordering in for $LaMnO_3$. (Taken from [17]).

Much of the challenge and interesting phenomenon, including the CMR effect starts to show up as soon as the parent compound is doped. However, many of the basic ingredients, such as orbital ordering and Jahn-Teller distortion, are already present in pure $LaMnO_3$ [18]. Thus, a complete understanding of the parent compound is a prerequisite to understanding fully the doped manganites. Owing to this reason a large number of theoretical investigations has already been undertaken on stoichiometric $LaMnO_3$.: using the LDA + U method [17, 19], and within the LSDA [12, 13, 20, 21]. It was shown that many properties such as the correct magnetic ground state are well described by these methods, provided that the correct experimental crystal structure is used in the calculations.

Earlier theoretical works focused on the undistorted cubic structure and it was found that the usual LSDA couldn't reproduce the observed insulating ground state for $LaMnO_3$ [25]. This is partly due to the absence of structural distortions in the cubic phase, which play a significant role in reproducing the insulating character of the material. Other theoretical calculations on the orthorhombic structure have used the experimental geometry so as to account for the role of structural distortion on the electronic and magnetic properties of the material. Nevertheless, the value of the insulating gap obtained from those calculations is rather very small when compared against the experimental value [16].

Therefore, a systematic study of the parent compound, especially, as to which the mechanisms are responsible in the stabilization of the insulating ground state, is still laking. Below is a very brief overview of two theoretical works, one on the cubic and the other on the orthorhombic phases of $LaMnO_3$.

Hill and Rabe [20] performed LSDA pseudopotential calculations to study the electronic and magnetic properties of $LaMnO_3$ in its high-temperature cubic perovskite structure. They used the experimental lattice parameter for the ideal cubic structure to calculate the electron band structures and densities of states with and without spin polarization. Figures 1.9 and 1.10 show the calculated densities of states and bands structures for the paramagnetic and ferromagnetic phases, respectively, of the cubic structure. From these results the authors were able to confirm that the paramagnetic phase is highly unstable and that a lower energy structure could be achieved by allowing spin polarization and/or structural distortion.

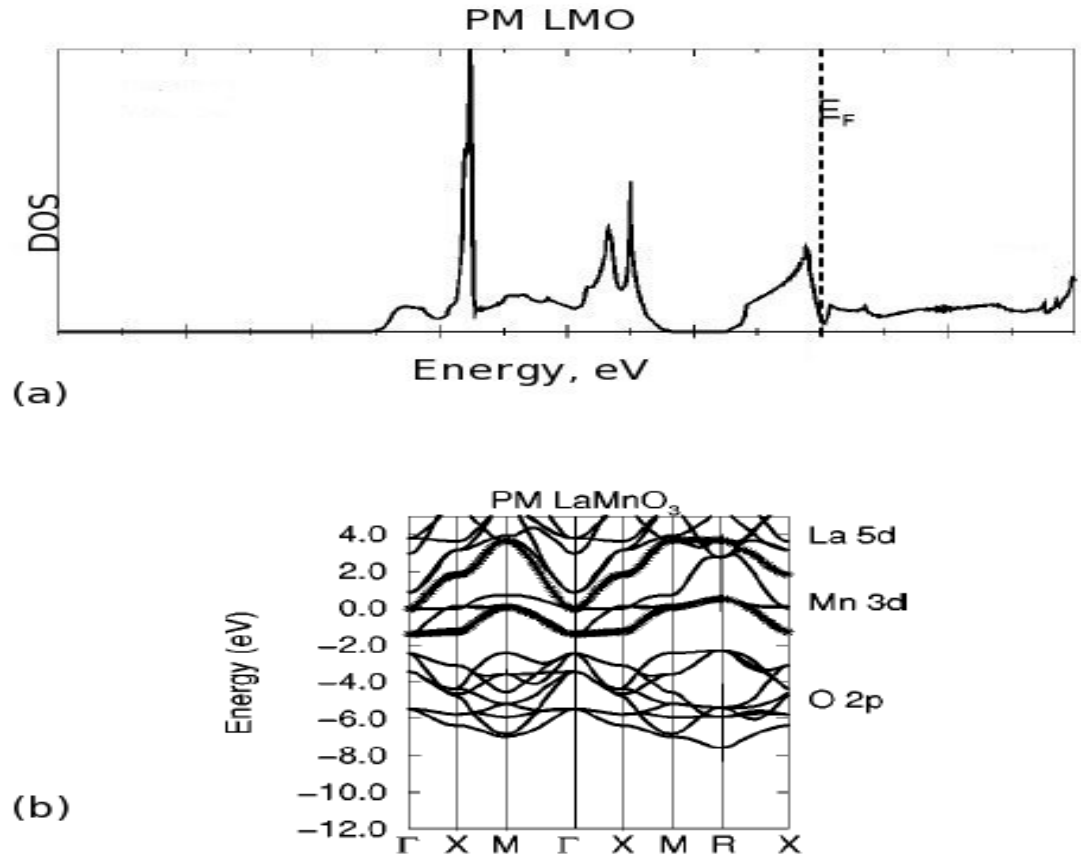

Figure 1.9. (a) Density of states and (b) Band structure of cubic paramagnetic $LaMnO_3$. (Taken from [21]).

The electronic-band structure for the ferromagnetic cubic phase obtained by the same authors is shown in Fig.1.10. Evidently, a simple metallic behavior is predicted by the band structure as electron bands from both the majority- and minority-spin channels cross the Fermi level . The authors also reported that they observed a 1eV reduction in the total energy of the system by introducing spin polarization.

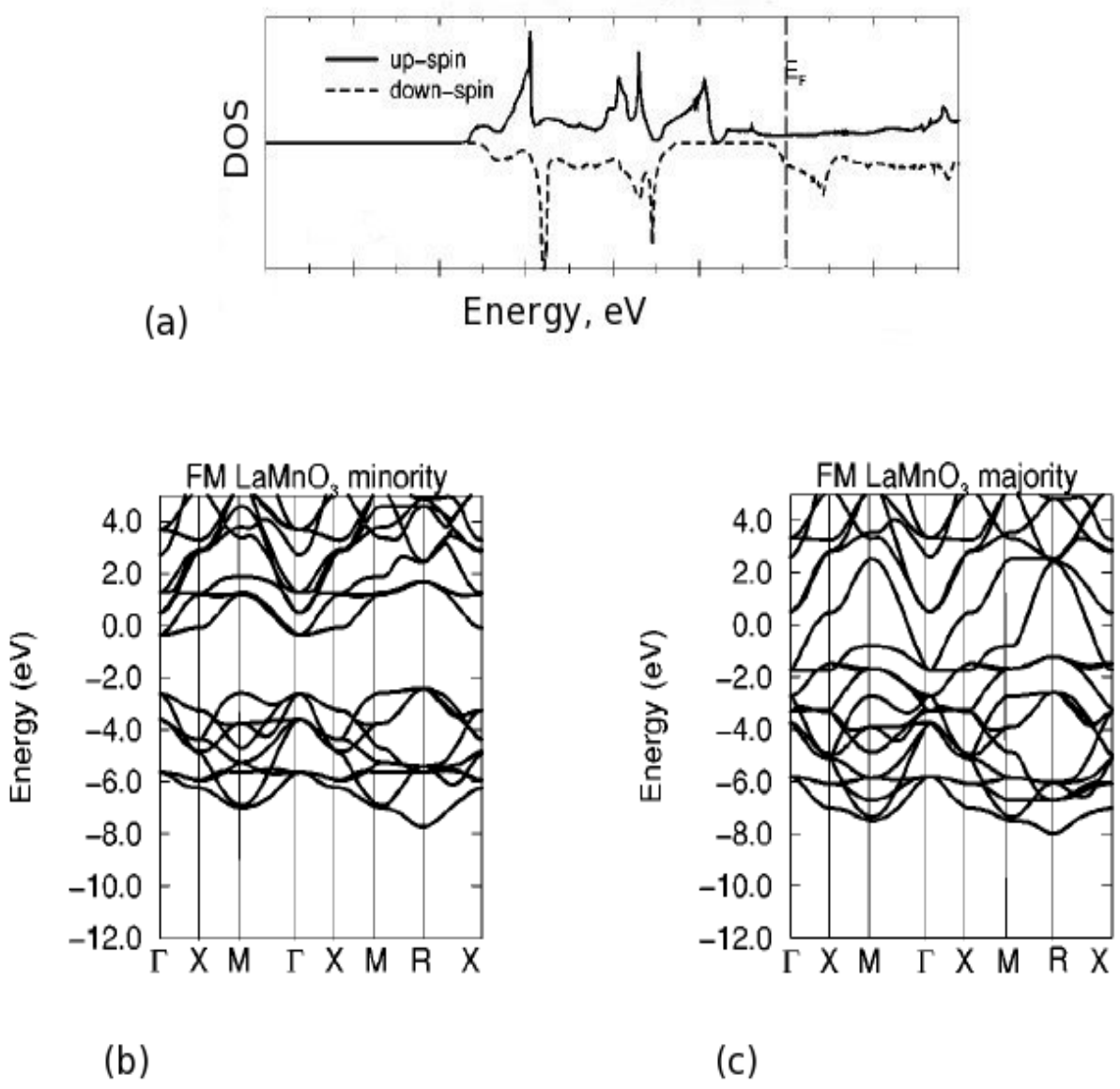

Figure 1.10. (a) Densities of states and (b) Electron band structures for the cubic ferromagnetic $LaMnO_3$. (Taken from [21]).

Mastrikov [16] used the experimental geometry for the orthorhombic structure with A-AF ordering to calculate the electronic band structures (see Fig. 1.11). The insulating gap obtained in this calculation is about 0.6eV, which is considerably smaller than the experimental value of 1.7eV. This, as pointed out by the author, is a typical underestimate of DFT calculations.

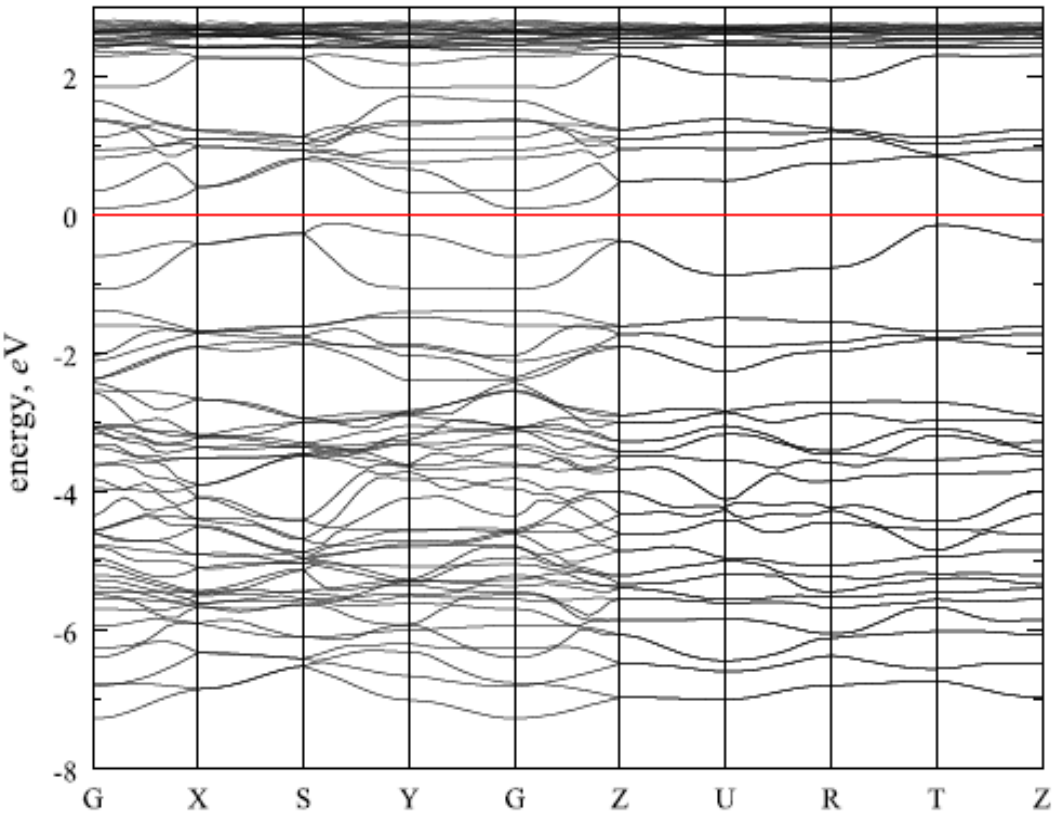

Figure 1.11. Band structure of orthorhombic $LaMnO_3$ in the A-AF phase. (Taken from [16]).

1.5 Objectives

1.5.1 General objective

The main objective of this thesis is to investigate the electronic, magnetic, and structural properties of pure $LaMnO_3$ using the quantum-ESPRESSO open-source code.

1.5.2 Specific objectives

The specific objectives of this thesis are:

- To investigate the role of on-site Coulomb interaction on the electronic and structural properties of $LaMnO_3$.
- To examine the phonon-dispersion curves and phonon density of states.
- To perform full structural relaxations for both the cubic and the orthorhombic crystals.
- To quantify the relative importance of electron-electron interaction and structural distortion to reproduce the insulating ground state for $LaMnO_3$.
- To develop a standard framework which can be used to study other members of the perovskite family.

1.6 Outline of the thesis

The rest of this thesis is organized as follows.

Chapter 2 is devoted to a discussion of the theoretical methods used in this work. Today the density functional theory (DFT) has already become a well-established theory. And hence, our aim here is to give a brief overview of theory and the standard approximations used in practical calculations. A detailed description of the method can be found in [26]. To deal with the role of electron correlation in $LaMnO_3$, the on-site coulomb interaction must be included. Therefore, a very brief discussion of the LDA+U method is also available in the chapter.

Chapter 3 contains a brief description of the computational procedure of the quantum-ESPRESSO code. The quantum-ESPRESSO is a freely available open source code, which is being used by researchers to study the properties of real materials from first-principles. The input file for a simple PWscf calculation is also discussed at the end of the chapter.

Our results are presented and discussed in chapter 4. Here, starting from the ideal cubic perovskite structure, we discuss the results of our first-principles calculations. Full structural relaxations have been performed for all the structure used in the calculations. Electronic-band structures and density of states are frequently used in our discussions.

Finally, the main results achieved in this thesis work are summed up in chapter 5.

CHAPTER 2

Theoretical background

2.1 Density functional theory

Numerous properties of real materials can now be determined directly from first-principles [23, 24, 25, 26], providing new insights into critical problems in physics, chemistry and materials science. The description of macroscopic solids from first-principles is based on the determination of the quantum mechanical ground state associated to their constituting electrons and nuclei. It consists in determining the quantum mechanical total energy of the system and in the subsequent minimization of that energy with respect to the electronic and nuclear coordinates (variational principle). This defines a complex many-body problem of interacting particles. Treating this problem within a full quantum-mechanical framework is almost impossible [27]. Hence, as one attempts to solve the problem, the usual choice is to resort to some sensible approximations (such as, the adiabatic approximation and the classical treatment of the nuclei).

Introduced by Hohenberg and Kohn [28], Density functional theory (DFT) [1, 26, 29, 30] has become one of the most successful first-principles theories. The method has been remarkably successful in predicting, reproducing, and as well as in explaining a wide variety of materials phenomena. It has proved to be highly successful in describing structural and electronic properties in a vast class of materials, ranging from atoms and molecules to simple crystals and complex extended systems [31].

The fundamental tent of DFT [32] is that any property of a system of many interacting particles can be viewed as a functional $F[\rho]$ of the ground state density of the electrons $\rho(r)$ [33]. This, the possibility to describe the ground state properties of a real system in terms of its ground state electronic charge density, is the first conceptual advantage introduced by DFT [34]. Which means that instead of seeking directly for the complex many-body wavefunctions of a system, we can adopt an intrinsically different point of view and consider the electronic charge density, a simple scalar function of position r, as a fundamental quantity of the problem. Another

key idea behind DFT is that a system of N interacting electrons in an external potential $V_{ext}(r)$ can be 'mapped' onto a system of N non-interacting Kohn-Sham electrons in an effective Kohn-Sham potential $V_{KS}(r)$ having the same ground-state charge density.

The true ground state energy of a system is a minimum of the functional $F[\rho]$ [33], and the density that minimizes the functional is the true density of the electrons in their ground state. For the fictitious Kohn-Sham system, the universal density-functional $F[\rho(r)]$ corresponds to the kinetic energy of the non-interacting electrons $T_0[\rho(r)]$. For the interacting electron system, $F[\rho(r)]$ can then be expressed as the sum of the kinetic energy of the non-interacting electron gas with the same density and the additional terms describing the inter-particle interaction:

$$F[\rho(r)] = T_0[\rho(r)] + \frac{e^2}{2}\int \frac{\rho(r)\rho(r')}{|r-r'|}drdr' + E_{xc}[\rho(r)] \tag{2.1}$$

where $\int \frac{\rho(r)\rho(r')}{|r-r'|}drdr'$ is the classical Coulomb interaction among the electrons, and $E_{xc}[\rho]$ is the exchange-correlation energy which accounts for all the many-body effects not described in the first two terms. The total energy functional of the original system of interacting electrons now becomes:

$$E = T + V + \frac{1}{2}\int \frac{\rho(r)\rho(r')}{|r-r'|}drdr' + E_{xc} \tag{2.2}$$

The effective Kohn-Sham potential $V_{KS}(r)$ is given by

$$V_{KS}(r) = V_{ext}(r) + \frac{\delta E_H[\rho]}{\delta\rho(r)} + \frac{\delta E_{xc}[\rho]}{\delta\rho(r)} = V_{ext}(r) + V_H(r) + v_{xc}(r) \tag{2.3}$$

To this end, we are left with the one-electron Schrödinger's-like Kohn-Sham equation:

$$\left(-\frac{1}{2}\nabla^2 + V_{KS}(r)\right)\psi_i(r) = \varepsilon_i\psi_i(r) \tag{2.4}$$

It then follows that, by solving the single-particle Kohn-Sham equations (Eq. (2.4)) of the

auxiliary system, one can determine the single-particle density of the interacting system:

$$\rho(r) = \sum_i f_i |\psi_i(r)|^2 \tag{2.5}$$

where f_i is the Fermi-distribution.

Eq. (2.4) has a form of nonlinear Schrödinger equation whose potential (see Eq.2.3) depends on its own eigenfunctions through the electron charge-density (Eq. 2.5) distribution. Once an explicit form for the exchange-correlation energy is available, the equation can be solved in a self-consistent way. That means, we adopt an iterative method which, starting from an initial guess for the wave functions and the potential, evolves both up to self-consistency [34].

As described, DFT is exact in principle, but approximate in practice. The problem lies in the fact that no explicit form is known for the exchange-correlation functional. And hence, some assumptions are needed in its definition so as to convert the theory into a useful tool for ab initio calculations. Once an accurate and reasonably easy-to-use approximation for this functional is available, the Kohn-Sham scheme constitutes a practical way to implement the DFT [29, 35]. By treating the kinetic and electrostatic energies exactly one hopes that the exchange- correlation part is only a minor contribution.

2.2 Approximations to the exchange-correlation energy functional

2.2.1 Local Density Approximation

The local density approximation (LDA) is the first and most widely used approximation to the exchange-correlation energy. This approximation is based on the assumption that the exchange-correlation energy of a real system behaves locally as in a uniform electron-gas having the same density. Within the LDA, the exchange-correlation (E_{xc}) has the form:

$$E_{xc}[\rho(r)] = \int \rho(r)\varepsilon_{xc}^{LDA}(r)dr \tag{2.6}$$

where $\varepsilon_{xc}^{LDA}(r) = \varepsilon_{xc}^{\text{hom}}[\rho(r)]$ is the exchange-correlation energy density of the homogeneous system assumed.

A formulation of the exchange-correlation functional depending only on the total electron density should give an exact description of real systems [33], however, the treatment of magnetic systems is much easier if the exchange-correlation energy functional is explicitly considered as dependent on the two spin populations separately. Then, LDA is extended to include spin-polarization and results in what is known as the local spin density approximation LSDA, which is the most general local approximation. It can be formulated in terms of either the two spin densities $\rho^{\uparrow}(r)$ and $\rho^{\downarrow}(r)$, or the total density $\rho(r)$ and the fractional spin polarization $\xi = \frac{\rho^{\uparrow}(r) - \rho^{\downarrow}(r)}{\rho(r)}$. In the LSDA, the Kohn-Sham equations are solved independently for electrons with different spin orientation.

LDA, because of the assumption of slowly varying density, works very well for free-electron-like metals and is strictly valid only if the charge density is slowly varying. Considerable effort has been exerted to cure some of the deficiencies. Now, many extensions are available which give improved accuracy for systems with strongly correlated electrons, such as the manganites.

2.2.2 Generalized gradient approximation

There are different techniques that go beyond the homogeneous electron gas approximation so as to overcome some of the deficiencies of the LDA. As a first alternative, but connected approach, is to build a "semi-local" functional that depends not only on the density at r but also on its gradient, or on higher order gradient extensions. Different forms have been proposed that are summarized under the label of Generalized Gradient Approximations. They are all based on a functional of the type [10, 31]:

$$E_{xc}^{GGA}[\rho] = \int \rho(r)\varepsilon_{xc}^{GGA}\left[\rho(r);\left|\nabla\rho(r)\right|\right]dr \qquad (2.7)$$

By including the gradient of the density in the exchange-correlation functional some non-locality is introduced to the previously local functional.

Standard DFT approximations (LDA, LSDA, GGA) often fail to correctly describe strongly correlated systems [34-37]. Theses systems contain localized, atomic-like electronic

states, typically originating from d or f atomic states, together with delocalized, band-like states originating from s and p states . The electrons in a strongly correlated system are localized in the same shell and subjected to strong Coulomb repulsion. In a homogeneous-gas treatment, the LDA does not distinguish electrons as separate entities in the electron gas, and the effects of localization of electrons are not reproduced. The LDA+U method, which takes into account the orbital dependence of the Coulomb and exchange interactions, is quite efficient to study the band structures of strongly correlated systems.

2.3 Basic idea of the LDA+U method

The main idea proposed by the LDA+U method is to correct the LDA or GGA approach so that it can approximately describe strong electronic correlations [37, 38]. This requires one to go beyond the electron-gas approximation used to model electron-electron interactions. Suppose that we have a system (strongly-correlated) with partially filled d-orbitals. The energy of the on-site Coulomb interaction between the d-electrons can be written in a Hubbard-like form [33, 37, 38] as $\frac{1}{2}U\sum_{i\neq j}\eta_i\eta_j$, where η_i are occupation numbers. We add this term to the LDA functional. However, the LDA functional already has some contribution coming from the interactions of electrons in the d-shell. The Hamiltonian operator corresponding to this interaction can be written as:

$$H = \frac{1}{2}U\sum_{i\neq j}\eta_i\eta_j \tag{2.8}$$

The expectation value of this operator in the LDA depends on the total number of electrons N in the d-shell. Therefore, we can write the interaction energy in the LDA as:

$$H = \frac{1}{2}U\sum_{i\neq j}\eta_i\eta_j = \frac{1}{2}UN(N-1) \tag{2.9}$$

In order to avoid over counting, this expression is subtract from the LDA functional to obtain:

$$E = E_{LDA} - \frac{1}{2}UN(N-1) + \frac{1}{2}U\sum_{i\neq j}\eta_i\eta_j \tag{2.10}$$

This is still a functional of the total density that depends on N occupation numbers as parameters. The corresponding orbital energies are the derivatives of the total energy with respect to these parameters:

$$\varepsilon_i = \frac{\partial E}{\partial \eta_i} \tag{2.11}$$

Inserting $N = \sum_i \eta_i$ into the functional (2.9), we can write

$$E_{LDA+U} = E_{LDA} - \frac{1}{2} U \sum_i \eta_i (\eta_i - 1) \tag{2.12}$$

The orbital energies become:

$$\varepsilon_i = \varepsilon_{LDA} - U\left(\eta_i - \frac{1}{2}\right) \tag{2.13}$$

This shows that the occupied orbitals (η=1) decrease their energies by $\frac{U}{2}$ while the unoccupied ones (η=0) increase their energies by the same amount making the difference between occupied and unoccupied d-orbitals exactly U.

The parameter U can be estimated using various approaches. In practice, however, it is much easier to make a choice in such a way that some physical properties (such as, lattice constants, band gaps, etc.) agree with experiment [33]. We follow this procedure the present work. We first calculated the lattice parameter of the cubic perovskite $LaMnO_3$ with different values of U. The one obtained with a U_{eff} =3.5eV is in excellent agreement with experiment. This same value of U_{eff} is used in the subsequent LDA+U calculations.

2.4 The plane wave pseudopotential method

The plane wave pseudopotential (PWPP) method is one of the most widely used implementations of DFT [31, 32]. In the PWPP method, plane wave basis set is used to expand the electronic wavefunctions and pseudopotentials to model the electron-ion interactions. Plane waves have many attractive features. They are simple to use, orthogonal by construction, and unbiased by atomic positions. PW basis set, in principle, is only complete in the limit of infinite number of plane waves. However, in practical calculations, we deal with a finite number of plane-waves and choose those contained in a sphere of maximum energy E_{cut}.

$$-\frac{1}{2}\nabla^2\left|K+G\right|^2 \le E_{cut} \tag{2.14}$$

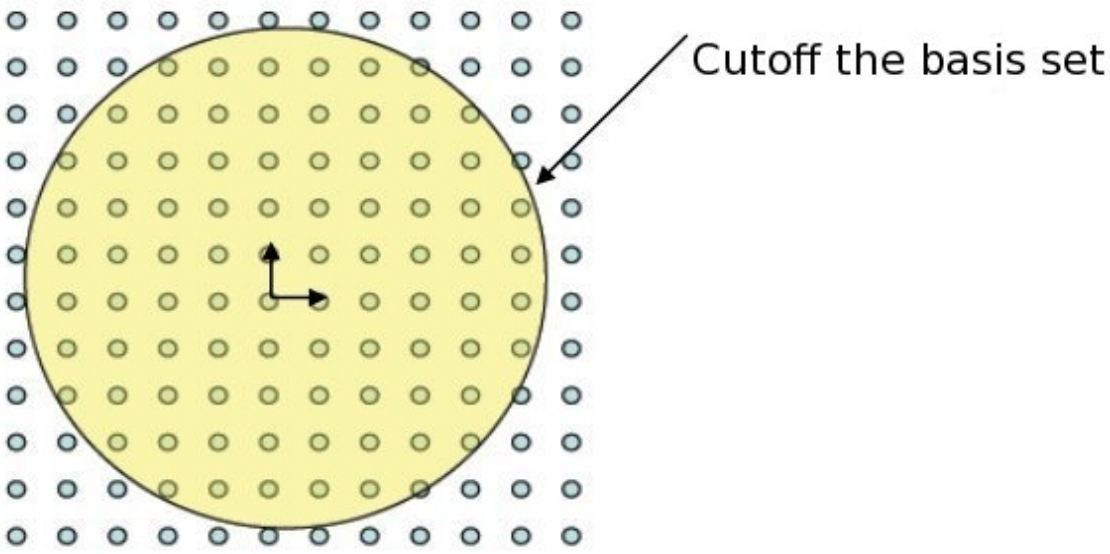

Figure 2.1. Uniform number of k points sampled in a sphere/circle.

Unlike calculations based on localized (atomic-like) basis sets, those made with plane waves can be simply checked for convergence by increasing the size of the basis set, as given by the kinetic energy cutoff. The energy cutoff is the only parameter in the theory, which controls the accuracy of the description of our system. The accuracy of the calculations can be improved by increasing the value of the energy cutoff and studying the convergence of the properties we are interested in. The especially important advantage of using PW basis set lies in the fact that the Pulay [39] terms are absent in the calculation of the derivatives of the energy. As a consequence, the Hellmann-Feynman expressions for force and force constants are valid without any correction [35, 39].

Plane waves are used in conjunction with pseudopotentials. Pseudopotential is an effective potential constructed to replace the atomic all-electron potential such that the core states are eliminated and the valence electrons are described by nodless pseudo-wavefunctions. The pseudopotential approximation, which is based on the assumption that the most relevant physical properties of a system are brought about by its valence electrons only, treats each nucleus together with its core electrons as a frozen core that doesn't change in response to changes in its environment. The valence electrons thus move in the effective external field produced by these inert ionic cores and the pseudopotential tries to reproduce the interaction of the true atomic potential on the valence states with out explicitly including the core states in the calculations. This provides a rational way to isolate the fundamental role of electrons in the electronic structure problem.

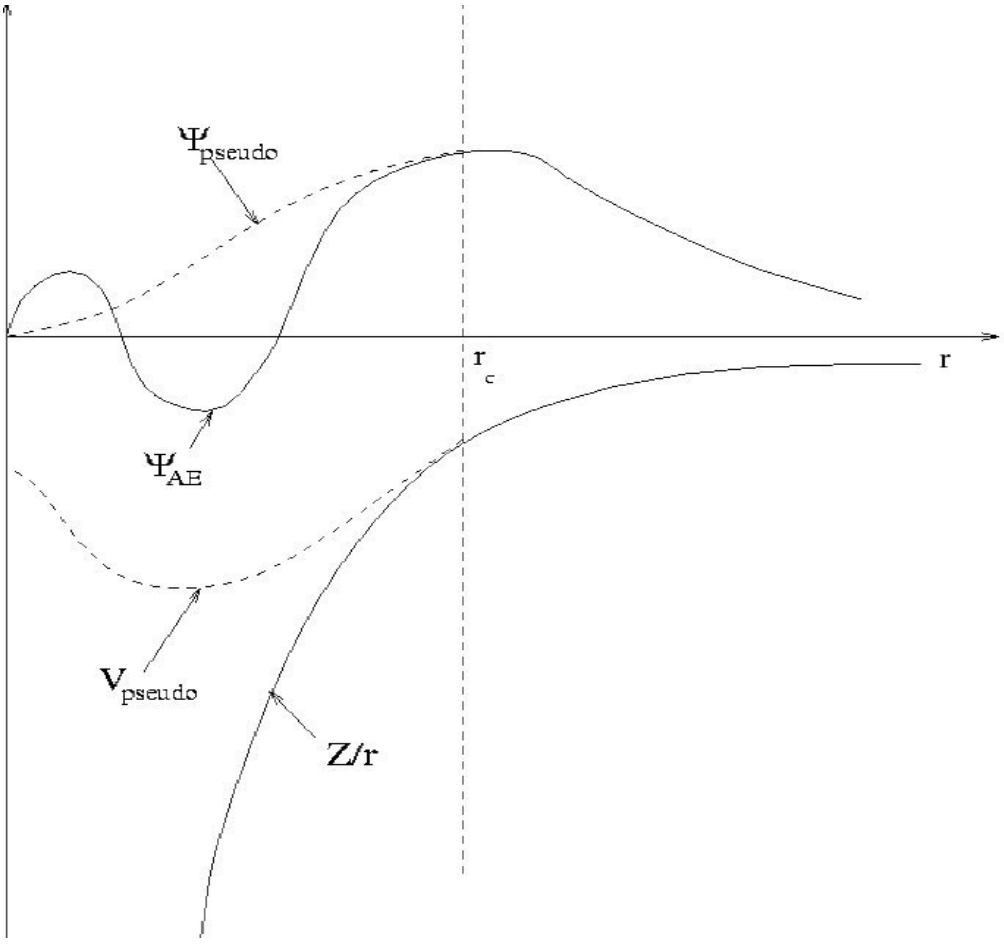

Figure 2.2. Sketch of the all-electronic wavefunction and electronic potential (solid lines) plotted against distance from the atomic nucleus. The corresponding pseudo wavefunction and potential (dashed lines) are plotted. Outside a given radius, r_c, the all-electron and pseudo electron values are identical.

CHAPTER 3

Computational methodology

3.1 Computational procedures of the quantum-ESPRESSO code

We used the Quantum-ESPRESSO (QE) open-source code to perform all the first-principles calculations presented in this thesis. QE is an integrated suite of computer codes for electronic structure calculations and materials modeling based on density-functional theory, plane-wave basis set and pseudopotentials to represent electron-ion interactions [40]. It is free software distributed under the terms of the GNU General Public License (GPL) [41]. The computational procedure of the QE code includes an iterative solution of the Kohn-Sham equations and optimized charge-density mixing routines. This includes the calculation of the Hellmann-Feynman forces acting on the atoms and the stresses on the unit cell. The total energy is optimized with respect to the positions of the atoms within a unit cell.

3.2 The Plane-wave self-consistent field method

As described in the second chapter, the set of Kohn-Sham equations is strongly non-linear and one has to adopt an iterative method in order to solve it.

The PWscf method implements an iterative approach to reach self-consistency, using at each step iterative diagonalization techniques, in the framework of the plane wave pseudopotential method. The procedure followed to do the self-consistent calculation is: one first makes a trial guess for the wave functions of all electrons and calculate its effective Kohn-Sham potential, V_{KS}. With this effective potential the Kohn-Sham equation is solved to get a new wave function. From these, a new V_{KS} is calculated, and so on. The procedure is terminated when the charge density does not vary much anymore. At this point self-consistency is reached, meaning that the wave function and the effective potential are self-consistent with each other, i.e. the wave functions correspond to those one would get from solving the Schrödinger equations with that potential. Both norm-conserving (NC) and ultrasoft (US) pseudopotentials are implemented in the PWscf method.

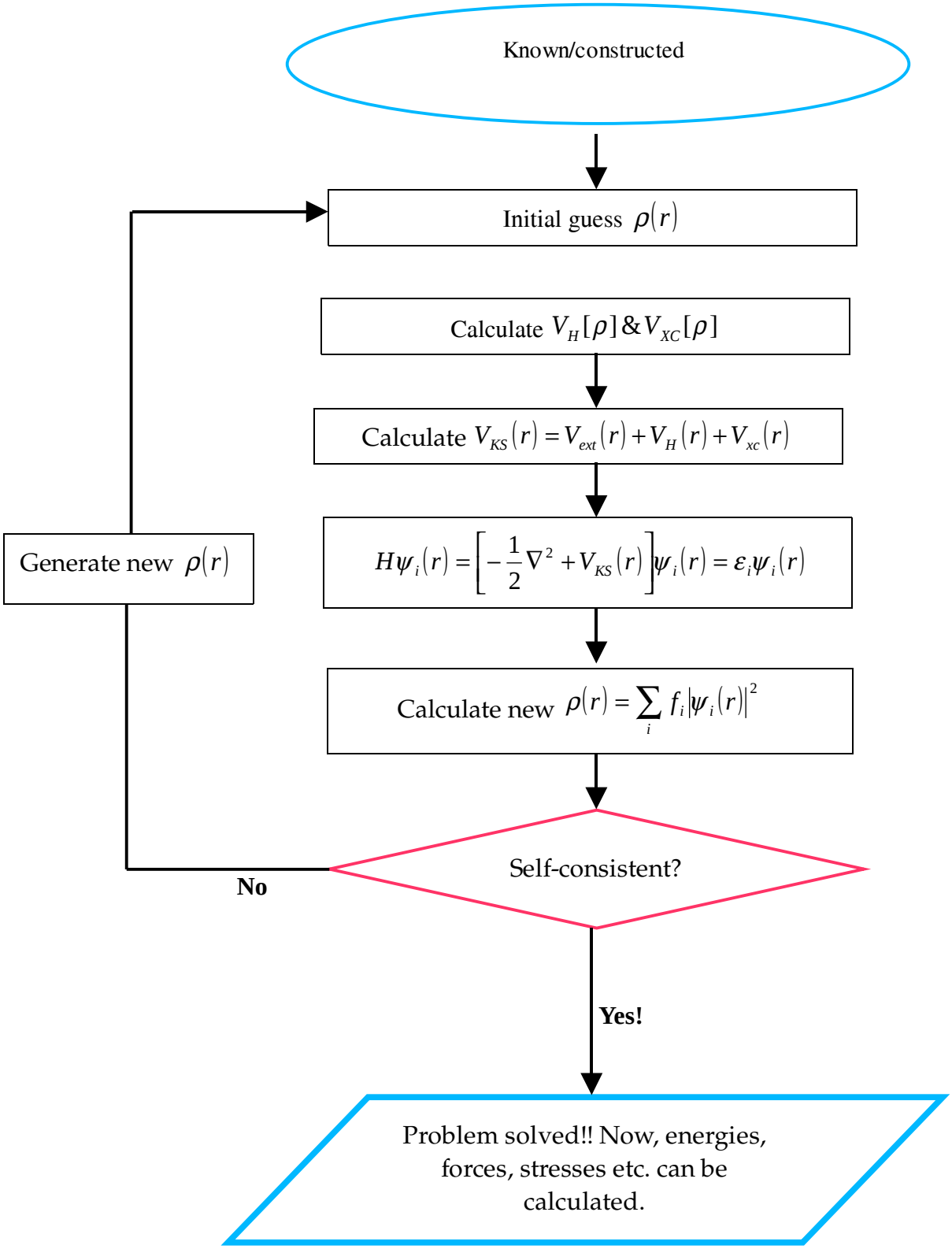

Figure 3.1. Calculation of the Kohn-Sham ground state.

3.3 Input file for a simple PWscf calculation

The input file for PWscf is constructed in a number of NAMELISTS and INPUT_CARDS.

The use of NAMELISTS allows specifying the value of an input variable only when it is needed and to define default values for most variable that then need not be specified. They are read in specific order and are ignored if not required. Three NAMELISTS are mandatory in PWscf. The first is &CONTROL which consists of the input variable that control the flux of the calculation and the amount of input/output on disk and on the screen. Input variables specifying the system under consideration are listed in &SYSTEM. The third mandatory NAMELIST is &ELECTRONS, which contains the input variables that control the algorithms used to reach the self-consistent solution of the Kohn-Sham equations for the electrons.

INPUT_CARDS on the other hand are used to provide input data that are always needed and would be boring to specify with the variable_name=variable_value syntax used by NAMELISTS. Similarly, there are three mandatory INPUT_CARDS. The name, mass, and pseudopotential used for each atomic species present in the system are specified in ATOMIC_SPECIES. ATOMIC_POSITIONS is where the type and coordinates of each atom in the unit cell are specified. K_POINTS the last mandatory INPUT_CARD that contains the coordinates and weights of the k-points used for the Brillouin zone integration. A typical input file for an scf calculation is shown bellow.

&CONTROL

calculation= 'scf'

pseudo_dir = '/home/MSC608/aqua/lab3/codes/espresso/pseudo',

outdir='/home/MSC608/Kal//cubic/ideal/temp'

prefix='lmo'

tstress = .true.

tprnfor = .true.

/

&SYSTEM

ibrav = 0 , celldm(1) = 7.50 , nat = 5 , ntyp = 3

ecutwfc = 30 , ecutrho = 300

nspin = 2, starting_magnetization(2) = 0.7

occupations = 'smearing', smearing='marzari-vanderbilt', degauss= 0.015

lda_plus_u=.true. , Hubbard_U(2)=3.5

/

&ELECTRONS

diagonalization='david'

startingwfc = 'atomic+random'

mixing_beta = 0.5

conv_thr = 1.0d-10

/

ATOMIC_SPECIES

La 138.9 La.pbe-nsp-van.UPF

Mn 54.94 Mn.pbe-sp-van_mit.UPF

O 15.9994 O.pbe-rrkjus.UPF

CELL_PARAMETERS (alat)

0.975769862 0.000000962 0.000000132

-0.000003547 0.975952249 0.000000169

0.000000129 0.000000172 0.977025891

ATOMIC_POSITIONS (crystal)

La 0.017624890 0.003736445 0.000004947

Mn 0.518452725 0.503153538 0.500004034

O 0.518945324 0.502829746 0.000004013

O 0.018493339 0.502741380 0.500003549

O 0.518952409 0.003128795 0.500003465

K_POINTS automatic

6 6 6 1 1

3.4 Computational details

The calculations in this thesis are performed within the generalized gradient approximation to the density functional theory (GGA) and LDA+U implemented within the PWPP method. Theoretically optimized structures are employed in these calculations for both the cubic and orthorhombic phases of $LaMnO_3$.

From convergence tests, cutoff energies of 30Ry and 300Ry are found sufficient for the plan-wave expansion of the electronic wavefunction and charge density, respectively. These values are quite moderate for we have used the Vanderbilt ultrasoft pseudopotentials, which, in addition to being less expensive, are known to be more accurate over a broad energy ranges. We used same cutoff energies for both the GGA and LDA+U calculations. As the electronic structure of the cubic phase turns out to be metallic, we adopted the marzari-vanderbilt smearing technique to smooth the Fermi distribution with a rather very small broadening width of 0.015Ry. Uniform meshes of 6 x 6 x 6 and 4x4x3 k-points are used in the Brillouin zone for the cubic and orthorhombic structures, respectively.

CHAPTER 4

Results and discussion

4.1 Cubic $LaMnO_3$

To start with, we consider $LaMnO_3$ in its ideal perovskite structure (fig. 4.1) for both paramagnetic (PM) and ferromagnetic (FM) phases. As described in the introduction, this is the high-temperature structure with five atoms per primitive unit cell stable above 750 K [16] with experimental lattice constant a_0= 3.95Å.

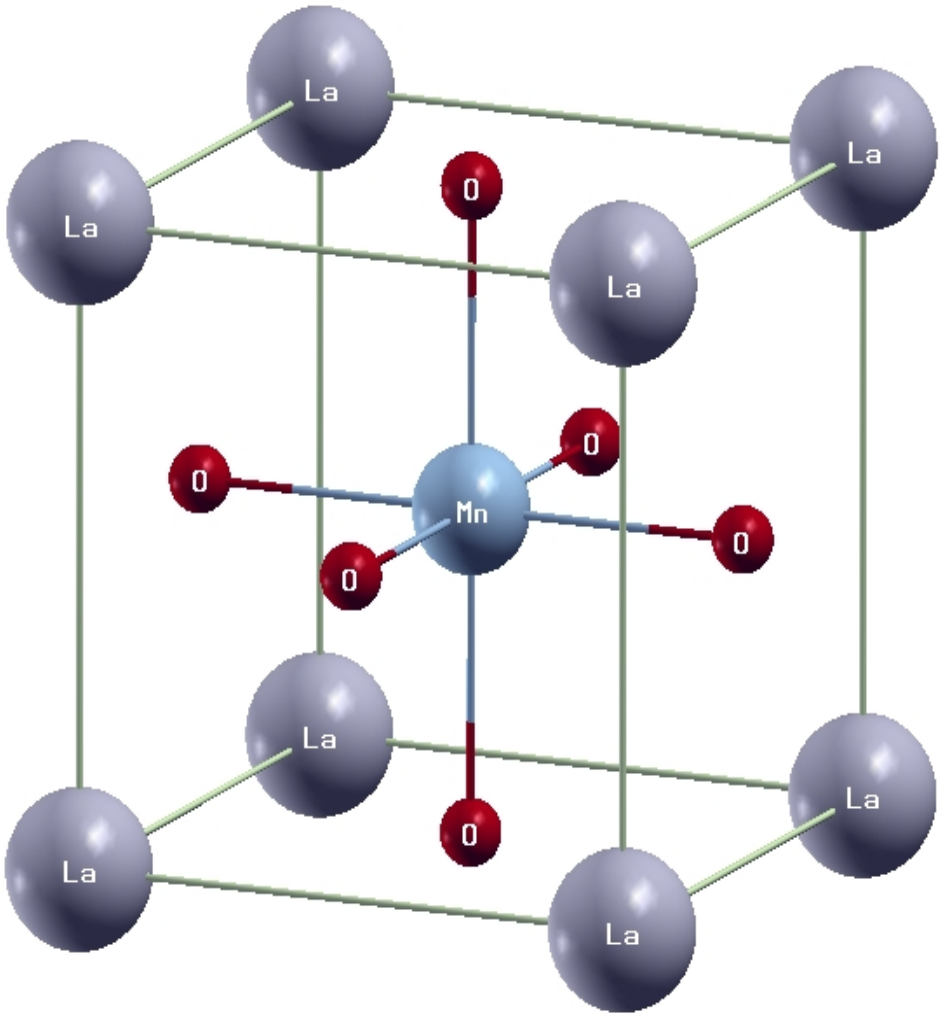

Figure 4.1. The ideal cubic perovskite structure of $LaMnO_3$.

4.1.1 Ideal cubic $LaMnO_3$

Fig. 4.2 shows the calculated densities of states for the PM and FM phases of the ideal perovskite structure. The Fermi level is set to zero. The large density of states at the Fermi level for the PM phase suggests that the cubic PM $LaMnO_3$ is highly unstable, and a lower energy state can be achieved by breaking the high magnetic symmetry.

The introduction of spin-polarization alone reduces the total energy of the system by around 1.2eV per unit cell compared with the unpolarized case. Thus, our results, in agreement with previous work [21], show that $LaMnO_3$ is a very favorable compound for cooperative magnetism. In fact, the calculated lattice constant for the paramagnetic state strongly deviates from experiment.

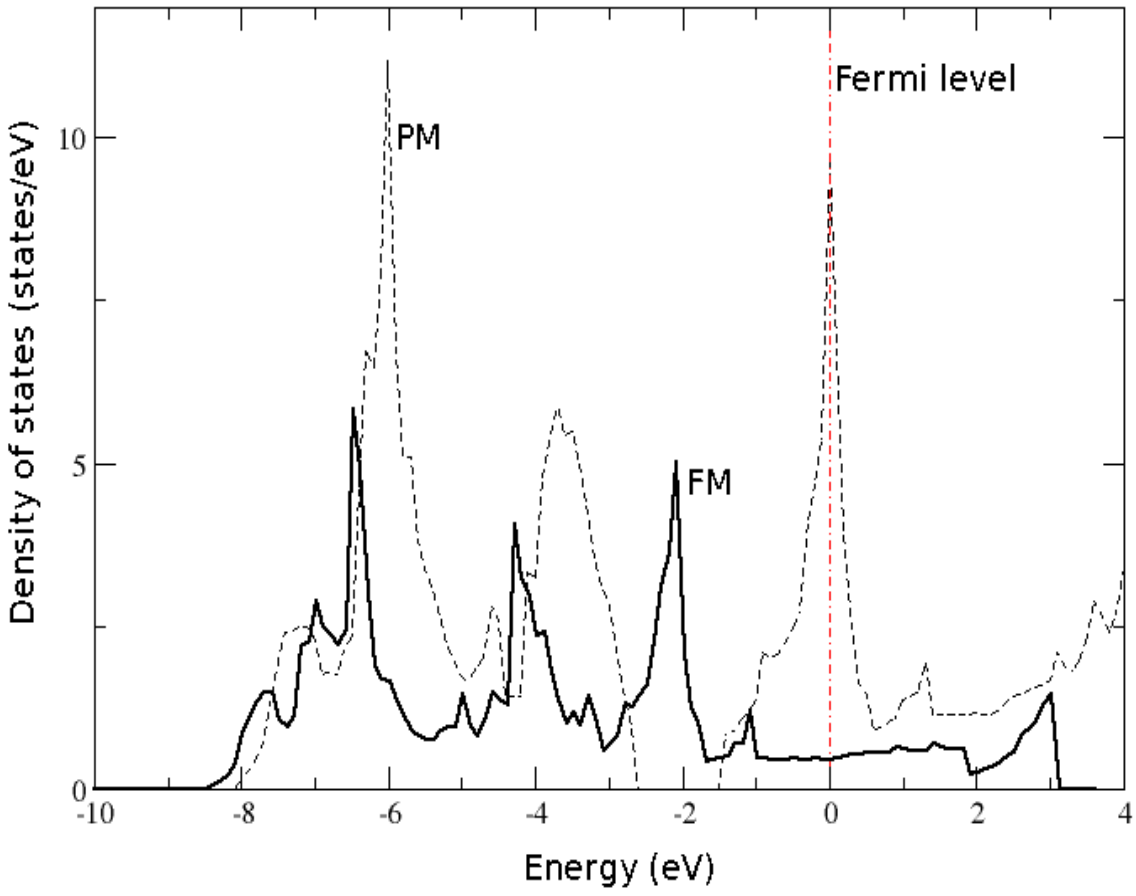

Figure 4.2. Calculated densities of states for the paramagnetic- (broken line) and ferromagnetic- (solid line) phases of cubic $LaMnO_3$. The Fermi level is set to zero.

Table 4.1. Total energies and lattice parameters for the paramagnetic and ferromagnetic phases of cubic $LaMnO_3$.

Phase	E (eV)	ΔE (eV)	a (a.u.)
PM	-5551.69	1.20	7.214
FM	-5552.89	0.00	7.401
Expt. [24]			7.494

The valence-band density of states of $LaMnO_3$ are derived primarily from Mn 3d and O 2p admixture with dominant Mn 3d character [42]. This in turn implies that the Mn 3d electrons play the dominant role in both the electrical conductivity and magnetism of the material. In the ideal cubic perovskite structure the 3d states of the Mn are split by the crystal field into the lower-lying threefold degenerate t_{2g} states and the higher-lying twofold degenerate eg states. According to the formal high-spin d^4 electron configuration of the Mn^{3+} cation, the majority-spin t_{2g} states are fully occupied, whereas the two majority-spin-e_g levels are filled with only one electron.

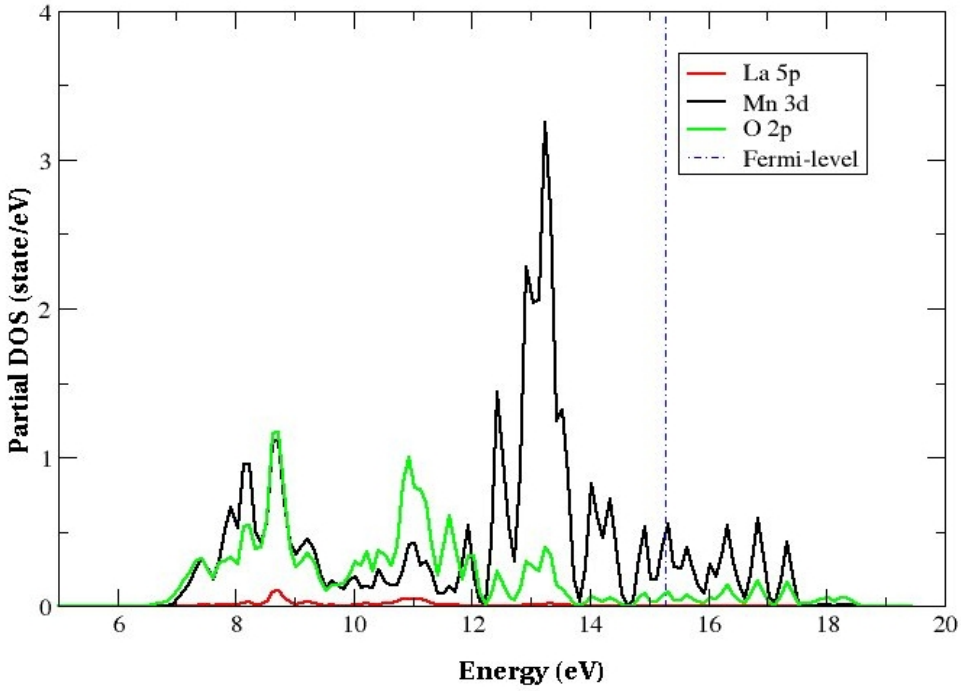

Figure 4.3. Partial densities of states for the cubic ferromagnetic $LaMnO_3$ within GGA.

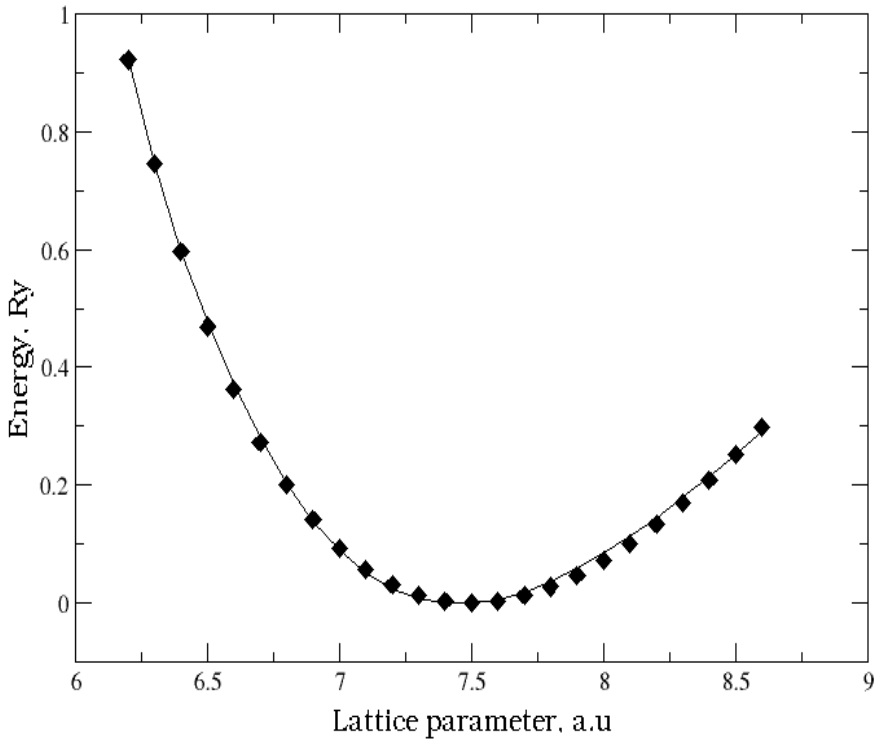

Figure 4.4. The total energy as a function of the lattice spacing and a Murnaghan-fit to the calculated points. The zero of the energy coincides with the minimum of the plot.

4.1.2 Theoretically optimized ferromagnetic $LaMnO_3$

Next, we performed a full structural relaxation for the FM phase in which both the microscopic (atomic coordinates) and macroscopic (shape and size of the unit cell) degrees of freedom are allowed to change. In the final relaxed geometry (nearly cubic structure) force components on each ion are bellow 10^{-3} $Ry/a.u.$ and the stress is 0.2kbar. The resulting lattice parameter for the relaxed structure is found to be much closer to experiment than what we obtained for the ideal structure.

The electronic band structures calculated for the theoretically optimized structure are shown in figs. 4.5 and 4.6. Here again, the cubic FM $LaMnO_3$ is predicted to be just a normal metal in which electrical conduction is possible by both spin channels: the Fermi level is being crossed by electronic bands coming from the valence manifold of both spin channels.

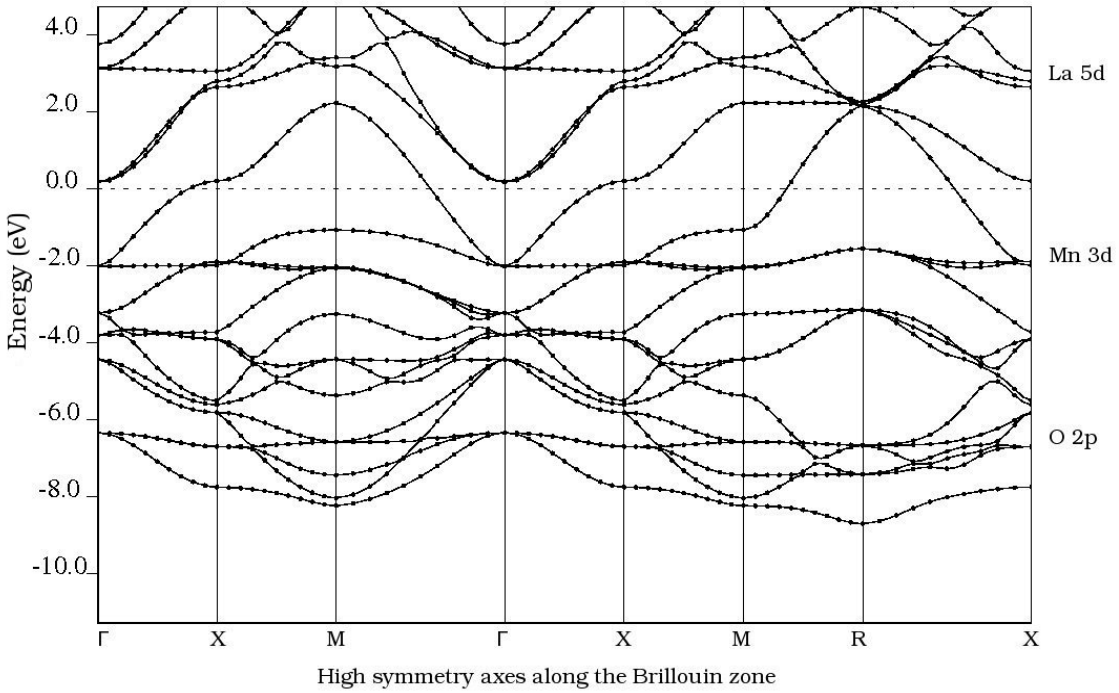

Figure 4.5. Calculated band structure of the majority- spin for cubic ferromagnetic $LaMnO_3$ obtained within GGA. The energy is normalized to the Fermi level (broken line).

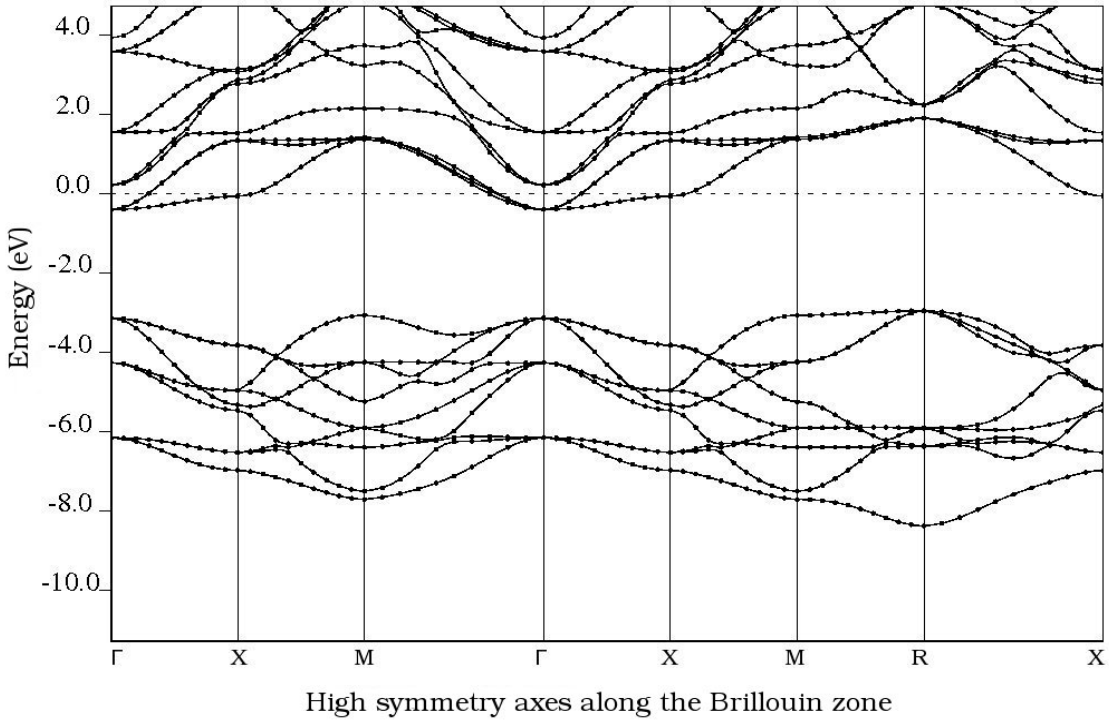

Figure 4.6. Calculated band structure of the minority-spin for cubic ferromagnetic $LaMnO_3$ obtained within GGA. The energy is normalized to the Fermi level (broken line).

The total density of states calculated for the same structure (Fig. 4.7) also confirms the same normal-metallic character. The majority-spin Mn 3d and O 2p bands undergo a strong hybridization, while the minority-spin Mn 3d band is split off from the O 2p band. Therefore, our calculations, in agreement with theoretical fact that the Mn in $LaMnO_3$ is in high-spin state, reproduce the spin dependence of the hybridization between Mn 3d and O 2p orbitals.

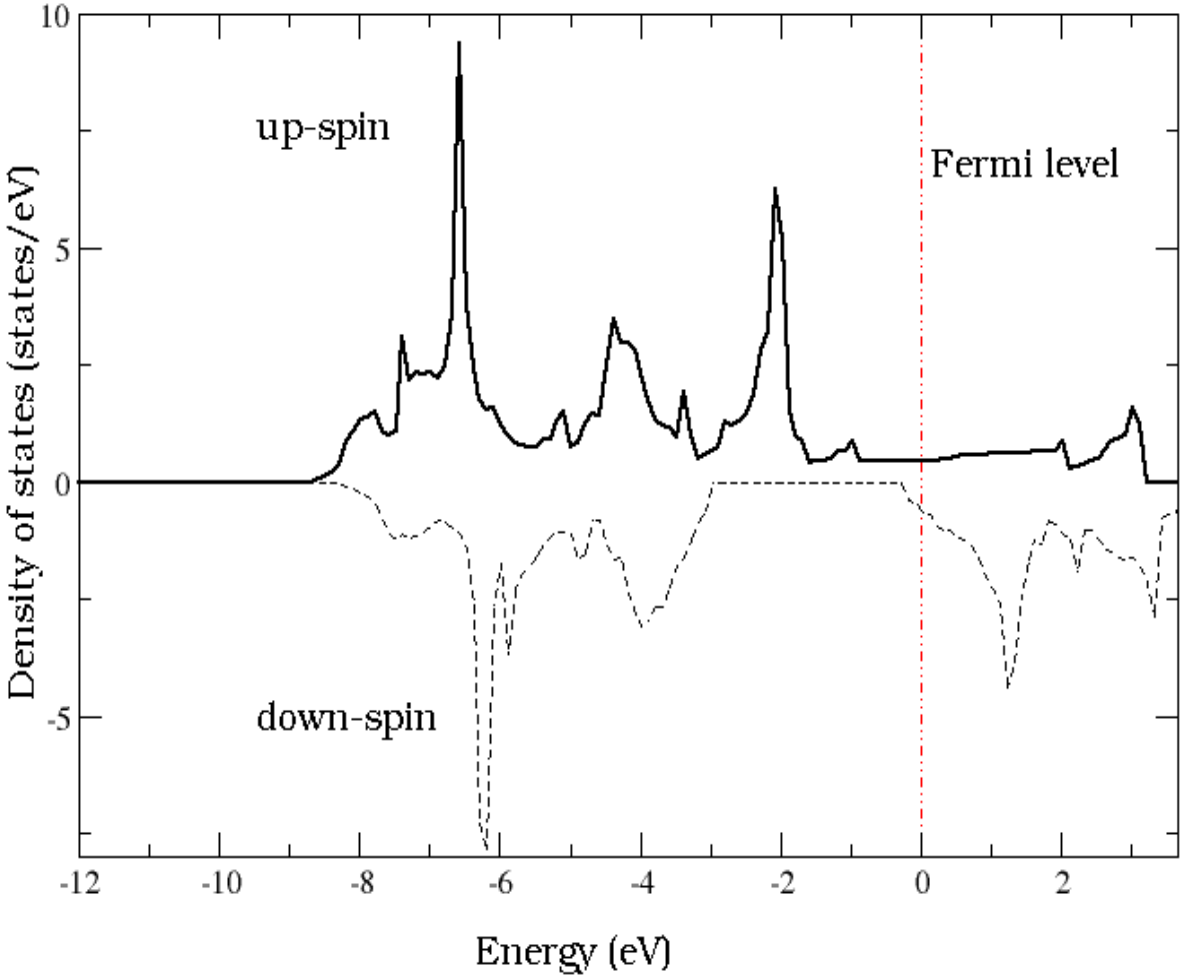

Figure 4.7. Calculated densities of states (DOS) for the ferromagnetic cubic $LaMnO_3$ obtained within GGA. The zero of the energy is set to the Fermi level of the system.

Previous DFT calculations show strong coupling between structural, magnetic, and electronic properties of the perovskite manganites. In order to study the role of electron-electron correlation in those properties of $LaMnO_3$, we have performed LDA+U calculations using U_{eff} = 3.5eV.

As we described, the procedure we followed in order to select the correct value of U_{eff} was to calculate the lattice constant of the ferromagnetic cubic phase with different values of U_{eff}. The result is shown in fig.4.4, where a fit of the calculated points to the Murnaghan equation of state is also introduced to estimate the equilibrium lattice spacing and bulk modulus.

A comparison with GGA (of this work) and experimental values for these quantities is presented in table 4.2. The lattice parameter and the magnetic moment obtained within the LDA +U are in a very good agreement with experiment. The electronic band structures for the majority- and minority-spin channels obtained at the theoretical geometry are shown in figs. 4.5 and 4.6. Comparing these plots with those shown in figs. 4.8 and 4.9, we can easily see that the introduction of spin polarization has caused a major change in the priority-spin channel. The electrons are now 100% spin polarized at the Fermi level and the system is predicted to be half-metallic. That is the most evident difference between the GGA and LDA+U results of the present work. Thus, perovskite $LaMnO_3$ exhibits the half-metallic character observed in the hole-doped lanthanum manganites. This adds to the evidence that most of the fundamental properties of the complex CMR manganites are already present in the parent compound.

High tunneling magnetoresistance is one of the most important manifestations of half-metallicity [43, 44]. This property means the Fermi level falls in the conduction band of one spin and in the gap of the other spin and thus the conduction electrons are expected to be of one spin component only since the system is insulating in the other component.

Table 4.2: The calculated lattice constant (a_0), bulk modulus (B_0), magnetic moment (μ_0) in comparison with GGA and experimental results.

	a_0(a.u.)	B_0 (Mbar)	$\mu_0(\mu_B)$
LDA+U	7.493	1.54	3.94
GGA	7.401	1.41	3.72
Expt. [24]	7.494	-----	3.80

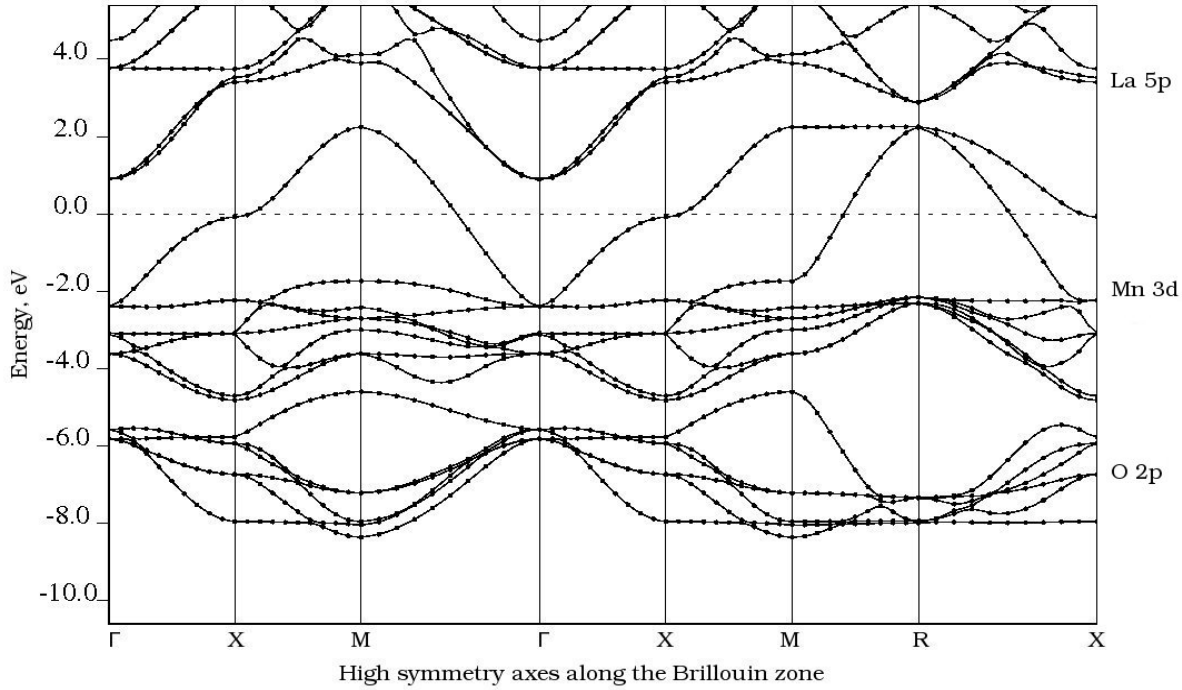

Figure 4.8. Calculated band structure of the majority-spin for FM cubic $LaMnO_3$ within LDA+U. The energy is normalized to the Fermi level.

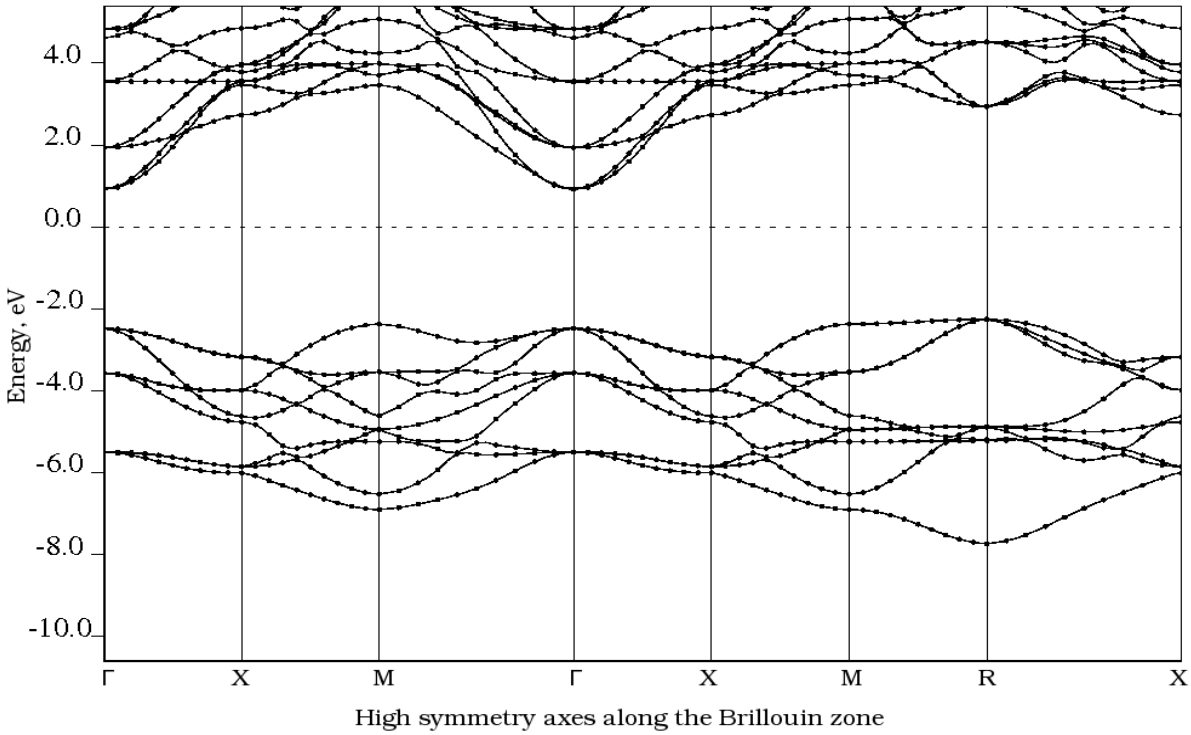

Figure 4.9. Calculated band structure of the minority-spin for FM cubic $LaMnO_3$ within LDA+U. The energy is normalized to the Fermi level.

In previous DFT calculations the half-metallicity $LaMnO_3$ was reported for the distorted orthorhombic structure only. Some authors [13, 21] have suggested that the different hybridization nature of the cubic and orthorhombic phases as well as the non involvement of the JT distortion in the cubic phase to be the possible reasons for the absence of the half-metallic character in those calculations for the cubic structure. This, however, is not the reason. Because the theoretically relaxed structure we used for our calculations is cubic which shows no asymmetry in the Mn-O bond lengths and the nature of the Mn 3d-O 2p hybridization remains nearly same before and after the introduction of U_{eff}. Therefore, our results clearly show that the Coulomb repulsion to be the factor responsible for the observed half-metallic character in the perovskite structure. Fig. 4.10 shows the total densities of states for the ferromagnetic cubic phase obtained within GGA and LDA+U. In agreement with the band structure calculations, in the case of the LDA+U, the DOS for the minority-spin is exactly zero.

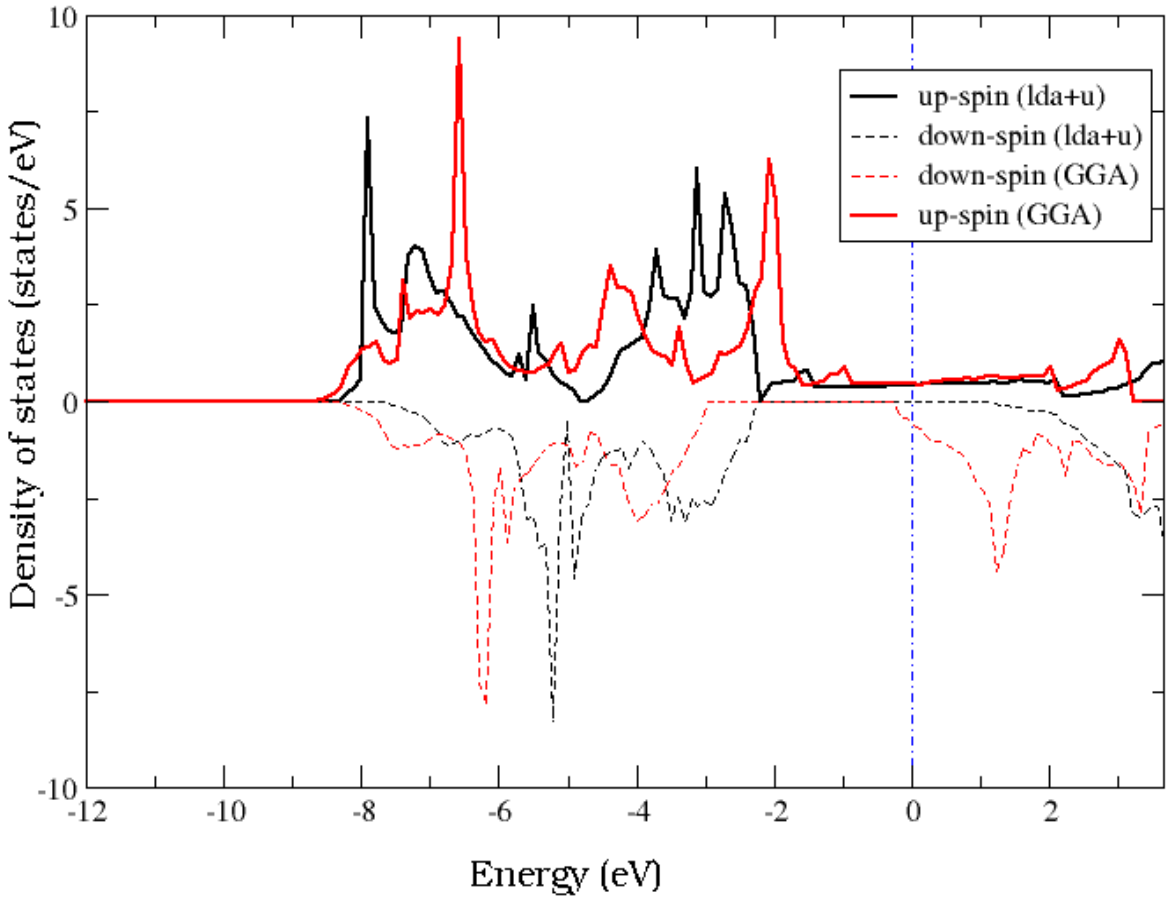

Figure 4.10. Densities of states calculated for the theoretically optimized cubic ferromagnetic $LaMnO_3$ obtained within the GGA and the LDA+U approaches.

4.2 Phonon dispersion

We have also calculated the phonon-dispersion curve for the relaxed ferromagnetic cubic $LaMnO_3$ at the theoretical lattice parameter. The phonon package in the computer code we used, Quantum-ESPRESSO, implements density-functional perturbation theory (DFPT) for the calculation of second- and third-order derivatives of the energy with respect to atomic displacements and electric fields. The perturbation theory approach allows the phonon frequencies at any **k** to be found from a calculation based on one unit cell [35].

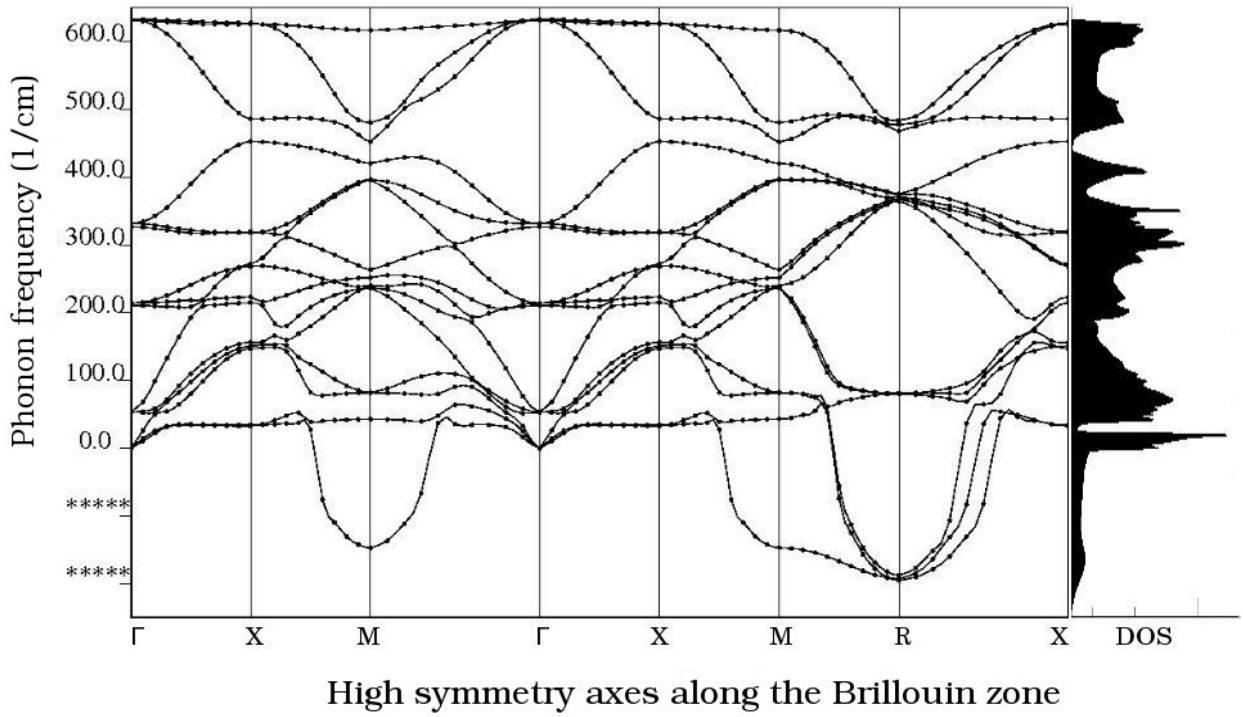

Figure 4.11. Calculated phonon-dispersion and density of states of ferromagnetic cubic $LaMnO_3$ obtained within GGA.

Our result for the phonon dispersion along high-symmetry axes of the Brillouin zone, together with the corresponding density of states, is depicted in fig. 4.10. Since there are 5 atoms in the cubic unit cell, there 15 phonon branches 3 of which are aquas tic and the remaining 12 optical. In its ground state, $LaMnO_3$ has a highly distorted orthorhombic structure. The orthorhombic distortion in the perovskites originates from the small volume of the La ion with respect to the volume of the holes between the octahedra in the undistorted cubic symmetry. The structural instabilities of the cubic structure are identified by the imaginary phonon frequencies, at M and R. The large negative frequency at R shows the major lattice instability in the system.

4.3 Orthorhombic $LaMnO_3$

As described in the introduction, $LaMnO_3$ in its ground state is stabilized in the orthorhombic structure. The exchange splitting owing to spin polarization, the crystal-field splitting of the t_{2g} and e_g states, and the further splitting of the twofold degenerate e_g orbitals by a strong Jahn-Teller distortion are among the most important factors that govern the formation of the structure of the orthorhombic $LaMnO_3$.

4.3.1 Ideal Orthorhombic $LaMnO_3$

The ideal perovskite structure has been the subject of most previous ab initio calculations without reproducing the correct insulating ground state. One of the main reasons for the failure of such calculations can be attributed to the absence of important lattice distortions in the cubic structure. In fact, it has been found that without lattice distortions $LaMnO_3$ would have a ferromagnetic ground-state, and even if forced to be A-AF it would still be metallic. We have calculated and compared the total energies for the F-, A-, C-, and G-AF phases of ideal orthorhombic $LaMnO_3$.

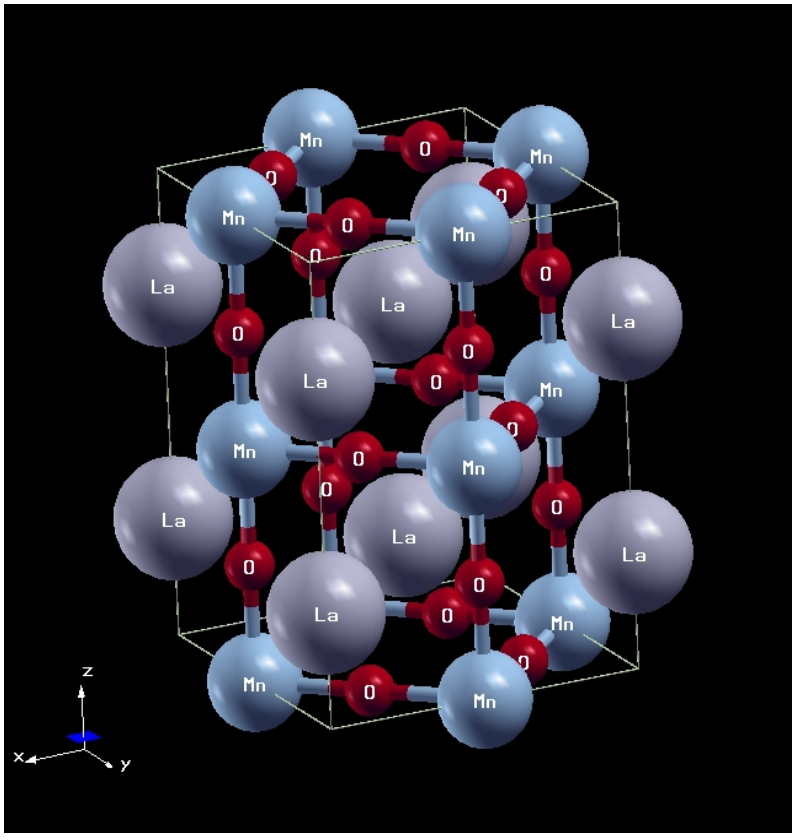

Figure 4.12. The orthorhombic unit cell (comprising 20 atoms) of $LaMnO_3$.

The calculations of Ravindran *et al* [36] for the orthorhombic structure using the experimental geometry show that the A-AF phase is 60meV above the FM phase. Our LDA+U calculations for the same structure show that the A-AF is only 54meV (Table 4.3) higher in energy than the FM phase. Therefore, our results for the undistorted structure agree with previous reports. The very small difference in the total energy of the A-AF and FM phase implies that a slight structural relaxation in the system can cause an abrupt phase change. We have calculated (fig. 4.13) the electronic band structure for A-AF magnetic ordering at the experimental lattice parameters. This can be used as a reference as we try to identify the changes in the electronic structure of the system, which are directly accounted for structural distortion.

From the fig. 4.13, we can clearly observe that a metallic character is exhibited. Thus, neither the inclusion of the on-site Coulomb interaction nor the implosion of the right, A-type, magnetic ordering is enough to open up the expected insulating gap. So, what remains to be checked is the structural relaxation and its role in reproducing the observed insulating character of $LaMnO_3$.

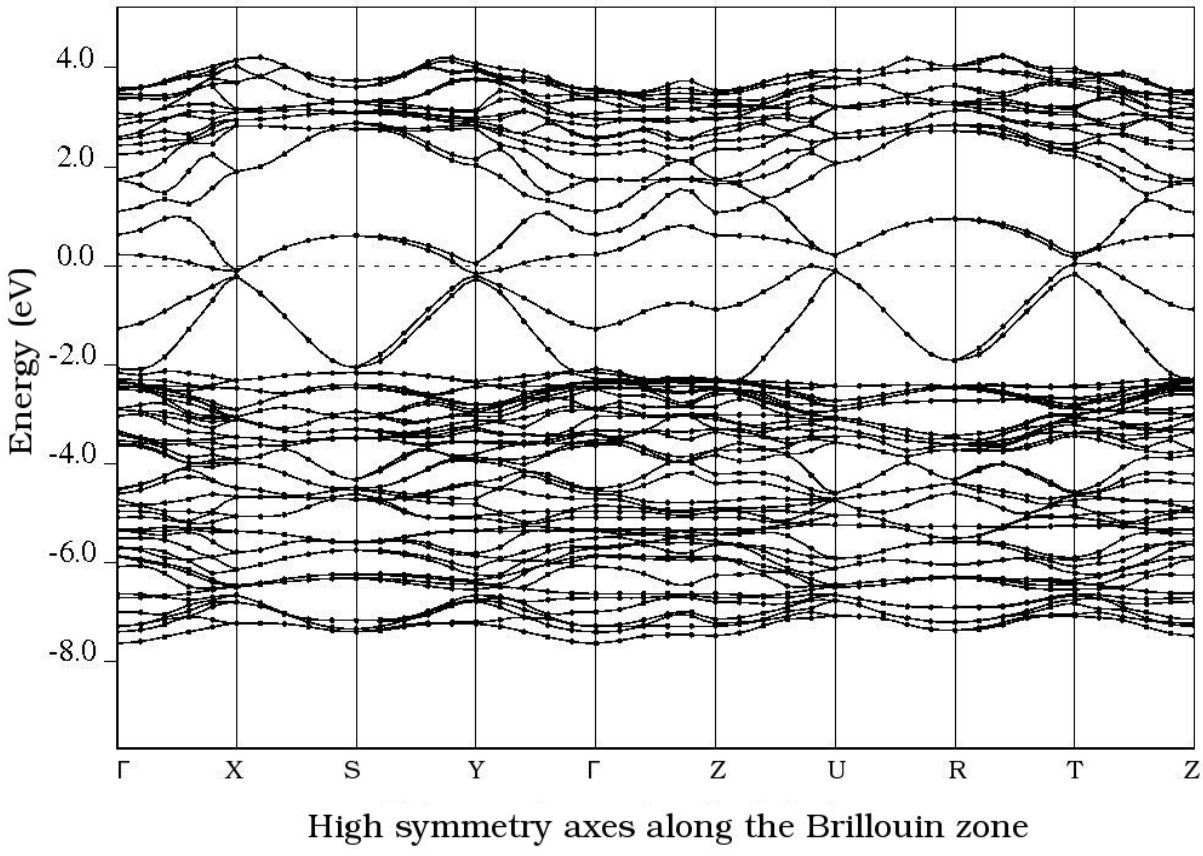

Figure 4.13. The electronic band structure of orthorhombic A-AF $LaMnO_3$ obtained within the LDA+U method at the experimental lattice parameters.

Table 4.3. Total energy (relative to the lowest-energy state) for $LaMnO_3$ in the four magnetic orderings with undistorted perovskite-like structure.

	FM	A-AF	C-AF	G-AF
E (meV/f.u.)	0.0	54	231	340
$\mu_0(\mu_B)$	3.90	3.80	4.12	4.01

4.3.2 Theoretically optimized orthorhombic $LaMnO_3$

We have performed full structural relaxations (vc-relax) of the 20-atom unit cell by imposing the A-AF magnetic ordering within both GGA and LDA+U. We have used a value of 3.5eV for the U_{eff}, the same value of that we and used for the calculations of the perovskite structure. It should be noted that no particular JT distortions were imposed in relaxations; rather we simply perturbed the system and left it alone to 'choose' its minimum-energy state. From DFPT we know that the equilibrium geometry of a system is determined by the condition that the forces acting on individual nuclei vanish. In the final relaxed geometry force components on each atom are well bellow 10^{-3} Ry/a.u.

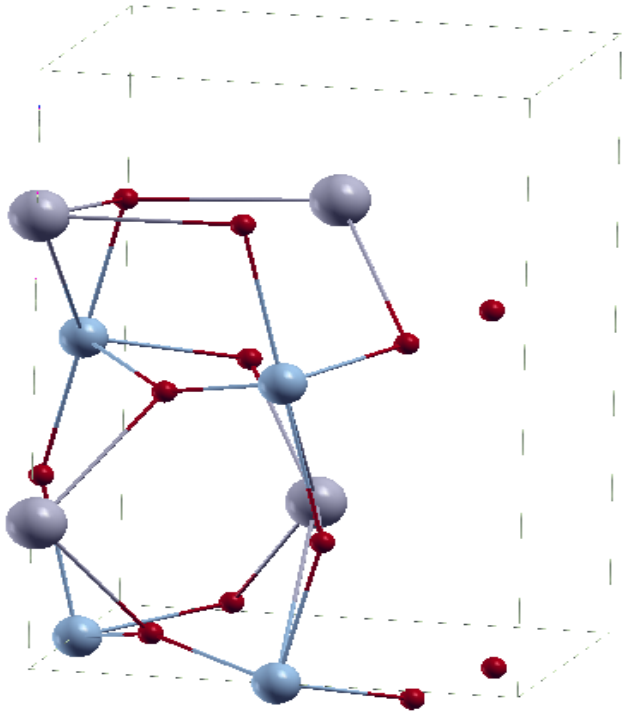

Figure 4.14. The theoretically optimized structure of orthorhombic $LaMnO_3$.

The calculated structural parameters and magnetic moments are compared with experiment in Table 4.4. Evidently, the structural parameters calculated within LDA+U are in excellent agreement, while the magnetic moment is overestimated. The GGA gives a better value of the magnetic moment as compared to the LDA+U.

Table 4.4. The lattice parameters and magnetic moment for the theoretically relaxed orthorhombic $LaMnO_3$.

	a(Å)	b(Å)	c(Å)	V(Å^3)	$\mu_0(\mu_B)$
Expt. [24]	5.5367	5.7473	7.6929	244.80	3.7±0.1
LDA+U	5.5439	5.7508	7.7102	245.82	4.01
GGA	5.4864	5.6949	7.6228	242.52	3.78
Ref. [45]	5.5612	5.7607	7.8083	250.12	3.83

Without hybridization the manganese spin moment is $4\mu_B$, which is the value one expects from having four d electrons localized (high-spin state). Owing to the covalent interaction between the Mn d and O 2p states the magnetic moment on the Mn can be less than 4.

As it was described in the introduction of this work, strong JT distortion as well as the mutual tilting and rotation of the MnO_6 octahedra characterize the orthorhombic structure. The JT distortion originating from the orbital degeneracy creates a local asymmetry in the Mn-O bond lengths. The Mn-O bond is modified from 1.97Å for the cubic case to 1.91, 1.96, and 2.18Å for the orthorhombic structure [26]. These are the short(s), medium (m), and long (l) bond lengths, respectively of Mn-O. The tilting of the octahedra on the other hand causes the Mn-O-Mn bond angle to be less than 180^0. We have observed a similar asymmetry in the Mn-O bond lengths in the fully relaxed structure obtained within LDA+U (see fig. 4.11). In agreement with a recent theoretical work [46], the short, medium, and long bond lengths we obtained for the fully relaxed structure within the LDA+U calculation are 1.93 Å, 2.08 Å, and 2.11Å. The average Mn-O-Mn bond angle for the same structure is 154^0. Comparing the calculated and experimental values we can safely conclude that the main features of the experimental structure can be reproduced with a proper structural optimization.

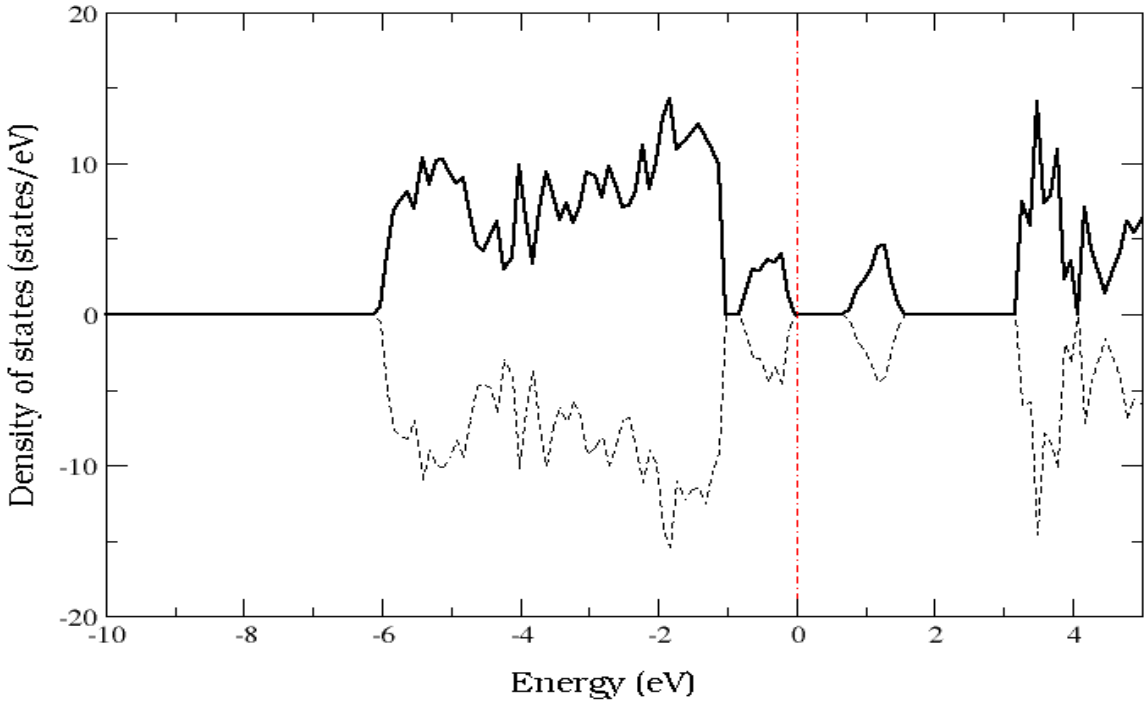

Figure 4.15. Total density of states for orthorhombic LMO in the A-AF magnetic ordering obtained within LDA+U. The zero of the energy is set to the Fermi level of the system.

Table 4.5: Energy ban gap for the orthorhombic $LaMnO_3$ with the A-AF magnetic structure.

	Expt. [27]	LDA+U	GGA	Ref. [16]
A-AF	2.0	1.1	0.52	0.60

Our GGA and LDA+U calculations for the theoretically relaxed structure have reproduced the insulating character of the material. The LDA + U results, as expected, are superior in quality as compared to those of the GGA ones. Fig. 4.15 shows the total density of states calculated for the relaxed structure. The energy is normalized to the Fermi level. The Fermi level lies in-between the occupied and unoccupied states. The band gap estimated from our DOS calculations is about 1.1eV. This insulating gap, though a much better estimate as compared to previous reports, is still far from the experimental value.

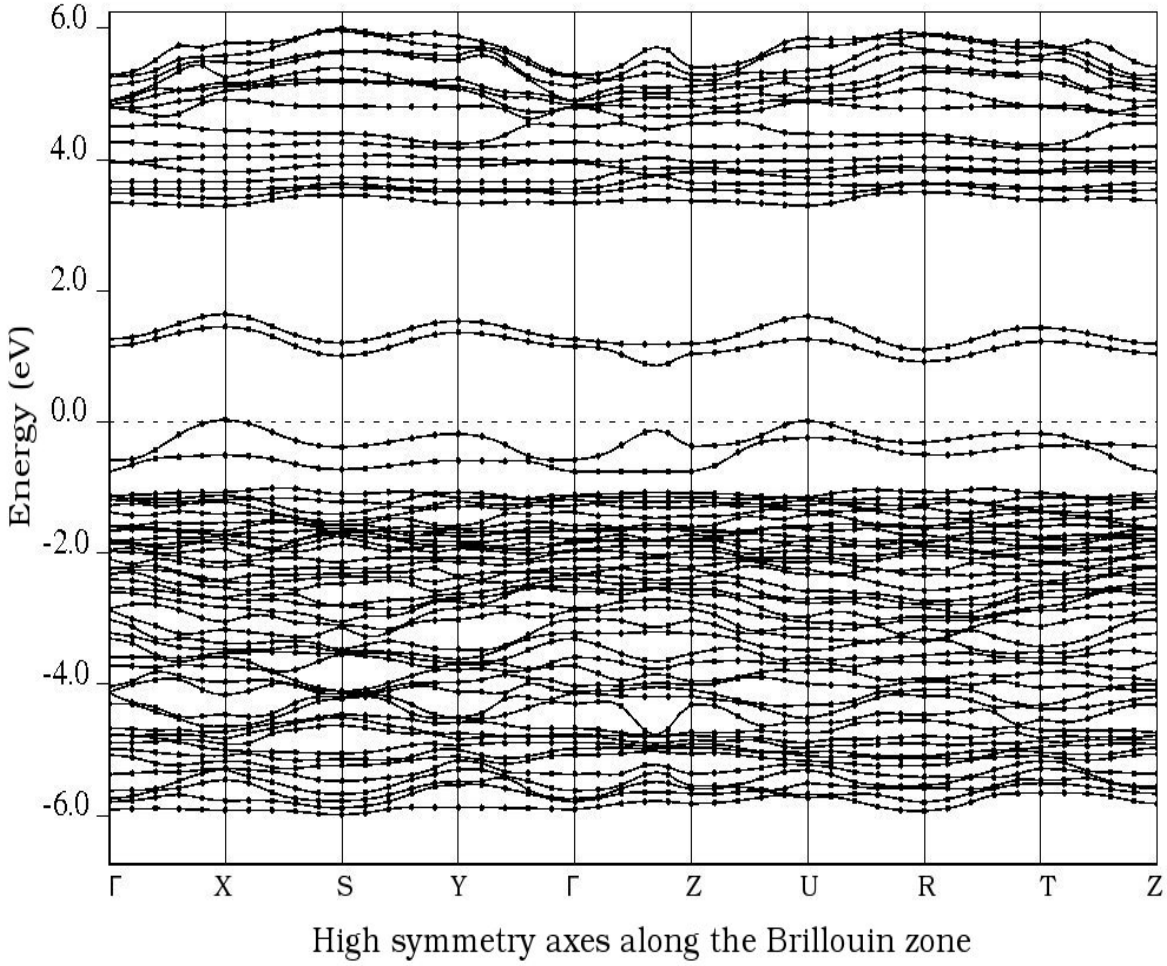

Figure 4.16. Calculated band structure for the theoretically relaxed orthorhombic $LaMnO_3$ with the A-AF magnetic ordering. The energy is normalized to the Fermi level (broken line).

Therefore, from the results of our band structure and DOS calculations it is evident that the insulating behavior of the $LaMnO_3$ is predicted by both the GGA and LDA+U approaches. A much better estimation of the insulating gap, however, is obtained only when the strong on-site coulomb interaction is explicitly considered.

Fig. 4.16 shows the electronic band structure for relaxed orthorhombic $LaMnO_3$ with the A-type magnetic ordering. It confirms the results we found from the DOS calculations for the same structure. One important feature of the band structure is the marked flatness of the bands, especially around the Fermi level. This means that, with the inclusion of the on-site Coulomb interaction, the electronic states (Mn 3d) around the Fermi level bands are rather localized.

CHAPTER 5

Conclusions

In this thesis, using the quantum-ESPRESSO package, we have performed first-principles calculations within the generalized gradient approximation to the density functional theory and LDA+U method to investigate the electronic structure as well as the magnetic and structural properties of the cubic and orthorhombic $LaMnO_3$. We have obtained the results for electron band structures, total and partial density of states, phonon-dispersion and the corresponding DOS.

For the perovskite cubic structure, our total energy and DOS calculations clearly show that $LaMnO_3$ is favorable to a spin-polarized approach as the paramagnetic phase is characterized by high DOS at the Fermi level. We observed a 1.2eV reduction in the total energy of the system by introducing spin polarization. We found nearly exact lattice spacing for the theoretically relaxed structure of the perovskite structure by considering spin-polarization and strong Coulomb interaction simultaneously. The electronic band structures for the theoretical structure obtained within LDA+U method shows half-metallicity, while the GGA results predict a simple metallic character. Unlike previous calculations, which consider structural distortion and nature of hybridization to be responsible for half-metallicity in $LaMnO_3$, our results show that the strong on-site Coulomb interaction is responsible for the observed half-metallic character. This is in agreement with the general theory of CMR manganites. The phonon-dispersion curve obtained for the fully relaxed cubic ferromagnetic phase shows that there are two strong lattice instabilities.

The insulating behavior in $LaMnO_3$ originates from the combined effect of crystal distortion and A-type antiferromagnetic ordering. Even though, a much better estimation of the insulating gap is obtained only when the on-site coulomb interaction is explicitly considered for the Mn 3d electrons. Moreover, without structural distortion $LaMnO_3$ is predicted to be metallic for all the possible magnetic orderings.

In conclusion, our LDA+U calculations, in addition to reproducing an improved insulating character for the orthorhombic phase, give a better description of the structural properties as compared to the corresponding results obtained within the GGA. One noticeable inconsistency to this general improvement is that the magnetic moments obtained within the GGA approach are

much closer to experimental values than those obtained within LDA+U.

Having showed that the quantum-ESPRESSO code, implementing the plane-wave pseudopotential (PWPP) method, can successfully be used to perform first-principles calculations to study systems complex as $LaMnO_3$, we strongly believe that the code can be used to study strongly correlated systems which are of current research interest for the huge technological potential they offer. Our method which we have implemented in this work can be used as a standard framework to calculate the electronic, magnetic, and structural properties of materials in the perovskite family and other related materials for which experimental data are not available.

References

1. W. G. Yin, D. Volja, and W. Ku, Phys. Rev. **96**, 116405 (2006).
2. L. P. Gor'kov and V.Z. Kresin, Phys. Rep. **400**, 149 (2004).
3. M. B. Salamon and M. Jaime, Rev. of Mod. Phys. **73**, 583 (2001).
4. T. V. Ramakrishinan, J. Phys.: Condens. Matter **19**, 125211 (2007).
5. T. Maitra, P. Thalmeier, and T. Chatterji, Phys. Rev. B **69**, 132417 (2004).
6. C. Ederer, C. Lin, and A. J. Millis, Phys. Rev. B **76**, 155105 (2007).
7. Y. Yang, PhD Dissertation: Dynamical mean-field theory for manganites (Stuttgart University, Germany, 2007).
8. M. J. C. Prieto, PhD Dissertation: Magnetic and electric properties of systems with colossal magnetoresistance (Institute of Ciencia, Madrid, Spain, 2001).
9. J. C. Chapman, PhD Dissertation: Phase coexistence in manganites (University of Cambridge, UK, 2005).
10. H. Zenia, PhD Dissertation: First-principles and model calculations of manganites (University of Sheffield, England, 2006).
11. K. Küpper, PhD Thesis: Electronic and magnetic properties of transition metal compounds: An x-ray spectroscopic study (University of Osnabrück, Osnabrück, Germany, 2005).
12. D. Munoz, N. M. Harrison, and F. Illas, Phys. Rev. B **69**, 085115 (2004).
13. P. Ravindran, A. Kjekshus, H. Fjellvag, A. Delin, and O. Erikson, Phys. Rev. B **65**, 064445 (2002).
14. L. Sheng, D. Y. Xing, D. N. Sheng, and C. S. Ting, Phys. Rev. Lett. **79**, 1710 (1997).
15. W. E. Pickett and D. J. Singh, Phys. Rev. B **53**, 1146 (1996).
16. Y. Mastrikov, PhD Dissertation: First-principles calculations of $LaMnO_3$ surface reactivity (Stuttgart University, Germany, 2008).
17. S. Satpathy, Z. S. Popovic, and F. R. Vukajlovic, Phys. Rev. Lett. **76**, 960 (1996).
18. M. Cestelli Guidi, G. Allodi, R. De Renzi, G. Guidi, M. Hennion, L. Pinsard, A. Amato, Phys. Rev. B **61**, 604 (2001).
19. Q. Qian, T. A. Tyson, S. Savarassov, C.-C. Kao, and M. Croft, Phys. Rev. B **68**, 014429 (2003).
20. N. A. Hill and K. M. Rabe, Phys. Rev. B **56**, 8759 (1999).
21. I. Solovyev, N. Hamada, and K. Terakura, Phys. Re. Lett. **76**, (1996).
22. N. N. Kovaleva, J. L. Gavartin, A. L. Shluger, A. V. Boris and A.M. Stoneham, J. Expt. Theor. Phys. **94**, 178 (2002).

23. H. Sawada, Y. Morikawa, K. Terakura, and N. Hamada, Phys. Rev. B **56**, 12154 (1997).
24. J. R. Carvaja, M. Hennion, F. Moussa, A.H. Moudden, L. Pinsard, and A. Revcolevschi, Phys. Rev. B **57**, R3189 (1998).
25. R. A. Evarestov, E. A. Kotomin, Yu, A. Mastrikov, D. Gryaznov, E. Heifets, and J. Maier, Phys. Rev. B **72**, 214411 (2005).
26. P. Ghosez and J. Junquera, Handbook of theoretical and computational nanotechnology (Stevenson Ranch, CA, USA, 2006).
27. J. Kohanoff and N.I. Gidopoulos, Density Functional Theory: Basics, New Trends and Applications (John Wiley&Sons, Ltd, Chichester, England, 2003).
28. P. Hoenberg and W. Kohn, Phys. Rev. **136**, B864 (1964).
29. G. Kresse and D. Joubert, Phys. Rev. B **59**, 1758 (1999).
30. M. M. Savosta and V. A. Borodin, Phys. Rev. B **59**, 8778 (1999).
31. N. A. Hill, Annu. Rev. Mater. Res. **32**, 1-37 (2002).
32. R. M. Martin, Electronic Structure: Basic Theory and Practical Methods (Cambridge University Press, England, 2005).
33. A. Malashevich, PhD Dissertation: First-principles study of electric polarization in piezoelectric and magnetoelectric materials (Rutgers University, New Jersey, USA, 2009).
34. M. Cococcioni, PhD Thesis: A LDA+U study of selected iron compounds (Trieste, Italy, 2002).
35. S. Baroni, S. de Girincoli, and A. D. Corso, Rev. of Mod. Phys. **73**, 515 (2001).
36. P. Ravindran, R. Vidya, H. Fjellåg, and A. Kjekshus, J. of Crystal Growth **268**, (2004).
37. V. I. Anisimov, F. Aryasetiawan and A. I. Lichtenstein, J. Phys.:Condens. Matter **9,** 767 (1997).
38. P. Matl, N. P. Ong, and Y. F. Yan, Phys. Rev. B **57**, 10248 (1998).
39. P. Giannozzi, Numerical methods in electronic structre (University of Udine, Italy, 2007).
40. P. Giannozzi *et al*, J. Phys.: Condens. Matter **21**, 395502 (2009).
41. http://www.gnu.org/licenses.
42. A. Y. Ramos, H. C. N. Tolentino, N. M. Souza-Neto, J. P. Itie, L. Morales and A. Canerio, Phys. Rev. B **75**, 052103 (2007).
43. T. V. Ramakrishinan, H. R. Krishinamurthy, S. R. Hassan, and G. Venketeswara Pai, Phys. Rev. Lett. **92**, 157203 (2004).
44. A. Ciucivara, B. Sahu, and L. Kleinman, Phys. Rev. B **77**, 092407 (2008).
45. E. G. Rini, M. N. Rao, S. L. Chaplot, N. K. Gaur, and R. K. Singh, Phys. Rev. B **75**, 214301 (2007).
46. G. Trimarchi and N. Binggeli, Phys. Rev. B **71**, 035101 (2005).

APPENDIX

A typical output file of an *scf* calculation

bravais-lattice index = 0

lattice parameter (a_0) = 10.4630 a.u.

unit-cell volume = 1688.3112 (a.u.)^3

number of atoms/cell = 20

number of atomic types = 6

number of electrons = 176.00

number of Kohn-Sham states = 106

kinetic-energy cutoff = 30.0000 Ry

charge density cutoff = 300.0000 Ry

convergence threshold = 1.0E-10

mixing beta = 0.4000

number of iterations used = 8 plain mixing

Exchange-correlation = SLA PW PBE PBE (1434)

celldm(1)= 10.463000 celldm(2)= 1.038000 celldm(3)= 1.389400

celldm(4)= 0.000000 celldm(5)= 0.000000 celldm(6)= 0.000000

crystal axes: (cart. coord. in units of a_0)

a(1) = (0.999701 0.001112 -0.015130)

a(2) = (0.000939 1.019120 -0.000386)

a(3) = (-0.021183 -0.000364 1.447056)

reciprocal axes: (cart. coord. in units 2 pi/a_0)

b(1) = (1.000522 -0.000916 0.014646)

b(2) = (-0.001088 0.981240 0.000231)

b(3) = (0.010461 0.000252 0.691211)

.

.

.

the **Fermi energ**y is 11.7504 eV

! total energy = -1632.78853587 Ry

Harris-Foulkes estimate = -1632.78853587 Ry

estimated scf accuracy < 4.6E-11 Ry

The total energy is the sum of the following terms:

one-electron contribution = -645.60880499 Ry

hartree contribution = 430.55550818 Ry

xc contribution = -362.91697734 Ry

ewald contribution = -1055.25833814 Ry

Hubbard energy = 0.44007643 Ry

total magnetization = 0.00 Bohr mag/cell

absolute magnetization = 16.40 Bohr mag/cell

convergence has been achieved in 21 iterations

Forces acting on atoms (Ry/au):

atom 1 type 1 force = -0.00028213 -0.00101575 -0.00031663

atom 2 type 1 force = 0.00026385 0.00103281 0.00028746

atom 3 type 1 force = 0.00031176 -0.00103589 0.00040325

atom 4 type 1 force = -0.00033768 0.00106748 -0.00035331

atom 5 type 2 force = -0.00001546 -0.00003082 -0.00000467

atom 6 type 3 force = -0.00002926 0.00002508 -0.00000577

atom 7 type 4 force = -0.00000794 -0.00002768 0.00002693

atom 8 type 5 force = -0.00001397 0.00001862 -0.00000079

atom 9 type 6 force = 0.00046074 0.00048034 -0.00266172

atom 10 type 6 force = -0.00041294 -0.00057110 0.00257915

atom 11 type 6 force = -0.00031156 0.00052113 0.00267181

atom 12 type 6 force = 0.00048733 -0.00052214 -0.00269072

atom 13 type 6 force = 0.00204611 -0.00217706 -0.00018958

atom 14 type 6 force = -0.00150450 0.00150640 -0.00014574

atom 15 type 6 force = -0.00134780 -0.00137028 -0.00017206

atom 16 type 6 force = 0.00172654 0.00204509 -0.00021607

atom 17 type 6 force = 0.00129700 0.00131433 0.00031970

atom 18 type 6 force = -0.00182785 -0.00195668 0.00018305

atom 19 type 6 force = -0.00197934 0.00213508 0.00017893

atom 20 type 6 force = 0.00147710 -0.00143897 0.00010681

Total force = 0.009111 Total SCF correction = 0.000009

entering subroutine stress ...

total stress (Ry/Bohr**3) (kbar) **P**= -0.17

-0.00001381 -0.00000007 0.00000069 -2.03 -0.01 0.10

-0.00000007 -0.00000950 -0.00000007 -0.01 -1.40 -0.01

0.00000069 -0.00000007 0.00001981 0.10 -0.01 2.91